Atmospheric Environment 363 (2025) 121613

Contents lists available at ScienceDirect

Atmospheric Environment

journal homepage: www.elsevier.com/locate/atmosenv

Characterizing the Saharan dust transported to the UK through lidar ratio, particle depolarization, and spectroscopic measurements

Avinash C. Yadav [a,*], Boyan Tatarov [a], Rui Song [b], Adrian Ghita [c], Detlef Müller [a]

[a] Department of Physics, Astronomy and Mathematics, School of Physics, Engineering and Computer Science, University of Hertfordshire, College Lane, Hatfield, AL10 9AB, Hertfordshire, United Kingdom
[b] National Centre of Earth Observation, Atmospheric, Oceanic and Planetary Physics, University of Oxford, Oxford, OX1 3PU, Oxfordshire, United Kingdom
[c] School of Life and Medical Sciences, University of Hertfordshire, College Lane, Hatfield, AL10 9AB, Hertfordshire, United Kingdom

HIGHLIGHTS

- First UK study combining 532 nm lidar with spectral analysis of Saharan dust.
- Lidar and depolarization ratios at 532 nm confirm the presence of Saharan dust.
- Spectral signatures improved aerosol typing even at low dust loading (AOD = 0.19–0.26).
- Results show advantages of spectroscopic lidars over traditional lidars.

GRAPHICAL ABSTRACT

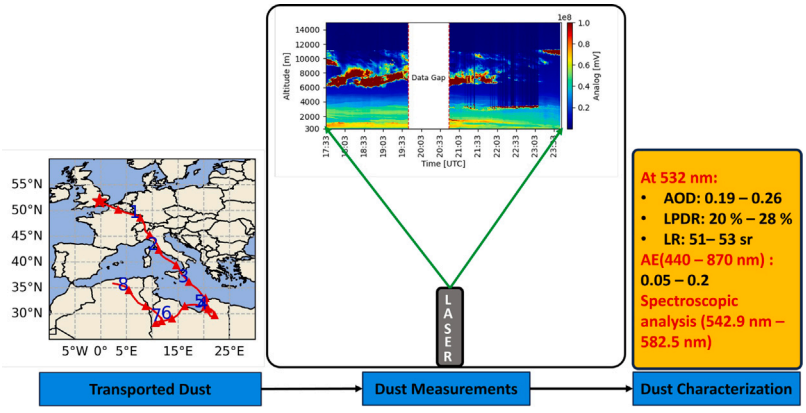

ARTICLE INFO

Keywords:
Saharan dust
Long-range transport
Lidar ratio
Particle linear depolarization ratio
Raman spectra
Spectroscopic lidar

ABSTRACT

On 1 May 2024, a Saharan dust plume was observed over Hatfield, UK, and analyzed using a novel spectroscopic lidar system (LITES) developed at the University of Hertfordshire. To the best of our knowledge, this represents the first coordinated study over the UK combining lidar optical properties at 532 nm with a spectrally resolved analysis of a long-range transported Saharan dust event. A distinct dust layer was observed between 2–5 km, with lidar-derived optical thickness values ranging from 0.19 to 0.26 at 532 nm, indicating a low-to-moderate Saharan dust intrusion. Within this layer, the lidar ratio was 53 ± 14 sr and the particle linear depolarization ratio was 0.27 ± 0.02, confirming the presence of non-spherical dust particles. After 4 h, despite the reduction in dust loading, the lidar ratios (mean: 51 ± 11 sr) and particle linear depolarization ratios (0.28 ± 0.01) remained characteristic of Saharan dust. Complementary AERONET observations, collected approximately 10 km from the lidar site, recorded low Ångström exponent values (0.05–0.2 at 440–870 nm) and a high total AOD of 0.5, with coarse-mode AOD contributing 0.37 (74%) at 500 nm, further confirming the dominance of coarse-mode Saharan dust. Spectrally resolved lidar signals revealed distinct Raman-shifted features near 571.0 nm ± 1.3 nm (1284 ± 40 cm^{-1}) and higher backscatter signals in the 542.9–554.4 nm (377-759 cm^{-1}) range, using a primary emission wavelength of 532 nm. These spectral features persisted throughout the dust layer but were absent in the Raman spectrum of a low-level cloud that was embedded in the dust layer during the lidar observation time. These dust spectral features furthermore disappeared above the dust layer, confirming their attribution to Saharan dust. The spectrally resolved observations are consistent with

* Corresponding author.
E-mail address: a.yadav@herts.ac.uk (A.C. Yadav).

https://doi.org/10.1016/j.atmosenv.2025.121613
Received 25 May 2025; Received in revised form 10 October 2025; Accepted 13 October 2025
Available online 17 October 2025

the Raman spectra of dust samples, which were measured in the LITES laboratory using Raman spectroscopy for direct comparison.

1. Introduction

Dust is one of the main components of atmospheric aerosol loading. It is estimated that dust particles account for about 75% of the global atmospheric aerosol mass load and 25% of the global aerosol optical depth (Kinne et al., 2006; Wu et al., 2020). The main sources of dust are the large arid areas distributed all over the world: the North African continent, the Arabian Peninsula, and the Asian continent (Prospero et al., 2002; Tegen and Schepanski, 2009). Dust originating from these arid regions can be transported over large distances by wind and convective processes. The Sahara Desert, the most significant contributor of the African region, contributes more than half of all global dust emissions (Yu et al., 2015; Gutleben et al., 2022). Saharan dust is frequently transported across the Mediterranean into Europe (Müller et al., 2009; Ansmann et al., 2003), toward Asia (Bi et al., 2024), and across the North Atlantic, reaching as far as the Caribbean (Gutleben et al., 2022; Liu et al., 2008) and South America (Kaufman et al., 2005; Weinzierl et al., 2017). Dust aerosols exert a wide range of direct and indirect effects on climate, the natural environment, and human health. These effects include altering the Earth's radiation balance, changing cloud and precipitation characteristics (Atkinson et al., 2013; Prenni et al., 2009), and modifying ocean and land biogeochemistry (Mahowald et al., 2005, 2009; Schepanski, 2018). Additionally, dust can adversely affect human health by degrading air quality and transporting pathogens (Prospero et al., 2014; Molesworth et al., 2003). Therefore, it becomes very important to characterize the dust particles in order to understand their multifaceted implications.

Long-range transport of desert dust mainly takes place in the free troposphere (Murayama et al., 2001; Mattis et al., 2002), which presents challenges for vertically resolved aerosol characterization with conventional passive remote sensing (Ansmann et al., 2003). While some space-borne instruments (e.g., MISR (Kahn et al., 2023)) and ground-based techniques (e.g., MAX-DOAS (Tirpitz et al., 2022)) can provide limited vertical information, their resolution remains insufficient for accurately characterizing elevated dust layers and retrieving range-resolved microphysical and optical properties. Furthermore, the coexistence of lofted dust plumes over areas with significant anthropogenic aerosol sources does not allow for accurate separation when observed by passive satellite or ground-based columnar measurements (Pérez et al., 2006). There is also a strong need for vertical profiling of dust to improve the understanding of dust advection on regional to intercontinental scales, its influence on radiative transfer, and its role in cloud formation (Tesche et al., 2009; Esselborn et al., 2009). Ground-based lidar measurements are strongly required, as they provide vertically resolved measurements of desert-origin aerosol properties at very high spatial and temporal resolutions.

It is well known that Europe receives a large amount of Saharan dust (transported across the Mediterranean Sea), primarily due to cyclonic activities inside and around the region (Dunion and Velden, 2004; Balis et al., 2006). Systematic lidar observations of Saharan dust vertical profiles over the European continent began with the establishment of the European Aerosol Lidar Research Network (EARLINET) in 2000 (Pappalardo et al., 2014). These observations have enabled the development of a substantial database of vertical profiles of Saharan dust optical properties. For example, Papayannis et al. (2008) presented a comprehensive study of the horizontal and vertical extent of Saharan dust intrusions over Europe for the time frame between May 2000 and December 2002, using coordinated lidar measurements within the framework of EARLINET. This effort was subsequently extended from 2006 to 2011, resulting in the longest time series analysis of vertical profiles of Saharan dust optical properties on a continental scale within the framework of EARLINET-ASOS (European Aerosol Research Lidar Network-Advanced Sustainable Observation System) (Pappalardo, 2007). Numerous dust outbreaks have been analyzed, revealing detailed insights into the geometrical, optical, and micro-physical properties of dust layers (Ansmann et al., 2003; Pérez et al., 2006; Müller et al., 2003; Soupiona et al., 2020). Recent studies across several European cities, employing the sophisticated EARLINET lidar network, have significantly contributed to our knowledge of dust transported over hundreds to thousands of kilometers (Zhang et al., 2022; Papanikolaou et al., 2024; Szczepanik et al., 2023).

However, systematic lidar-based dust characterization over the UK remains limited, with only a few investigations utilizing 355 nm lidar measurements to investigate its vertical distribution (Papayannis et al., 2008; Osborne et al., 2019). This reflects a broader lack of systematic lidar observations in the region, resulting in gaps in long-term monitoring and comprehensive analysis. To the best of our knowledge, the results shown in this contribution represent the first coordinated study in the UK combining traditional lidar-derived optical properties at 532 nm with spectroscopic analysis of a long-range transported Saharan dust event. The spectroscopic lidar measurements were further supported by complementary Raman spectra of various dust samples that we measured under controlled laboratory conditions, which allowed for the cross-validation of the observed spectral signatures. This integrated approach allows for the simultaneous retrieval of dust optical properties and compositional signatures. This methodological approach offers the opportunity for more accurate discrimination of dust layers under complex atmospheric conditions, particularly in dust-cloud mixed scenarios. Such characterization delivers a more complete description of aerosol properties in the region and represents an advancement over a solely optical parameters approach. Furthermore, these observations are essential for assessing the impact of transported dust on regional air quality and radiative balance, as well as for reducing uncertainties in aerosol radiative forcing and improving climate model performance. Accurate aerosol characterization requires well-defined aerosol types with distinct optical properties. Key lidar-derived parameters, such as the lidar ratio (extinction-to-backscatter ratio) and the particle linear depolarization ratio, provide information on particle size distribution, shape, and absorption efficiency. This methodology, which has been established for many years, allows for differentiation between dust, smoke, marine aerosols, and their mixtures. Significant progress has been made in regard to aerosol characterization in recent years (Kong et al., 2022; Floutsi et al., 2023). One of the next steps in further improving aerosol characterization lies in the complementary spectral analysis of lidar signals, as it further strengthens this aerosol classification by providing information on the chemical composition of dust particles in particular, but also aerosol particles in a more general context for future work.

A dust event was observed between 1–2 May 2024 over the southern part (Hatfield) of the UK. This dust case presented one of the first opportunities to observe and characterize dust properties over the UK using a novel spectroscopic lidar instrument at the University of Hertfordshire. We carried out a comprehensive analysis of the dust plume using our lidar, complemented by satellite data, AErosol RObotic NETwork (AERONET) observations, Copernicus Atmosphere Monitoring Service (CAMS) dust observations, and Hybrid Single-Particle Lagrangian Integrated Trajectory (HYSPLIT) modeled backward trajectories. First, the aerosol layer estimated by the model was identified by employing AERONET measurements, air-mass trajectory analysis, and lidar backscattering signals. Finally, the dust plume was characterized using the lidar ratio and particle linear depolarization profiles for two selected time periods. These time periods were selected based on data quality (cloud freeness and night-time). To refine the compositional

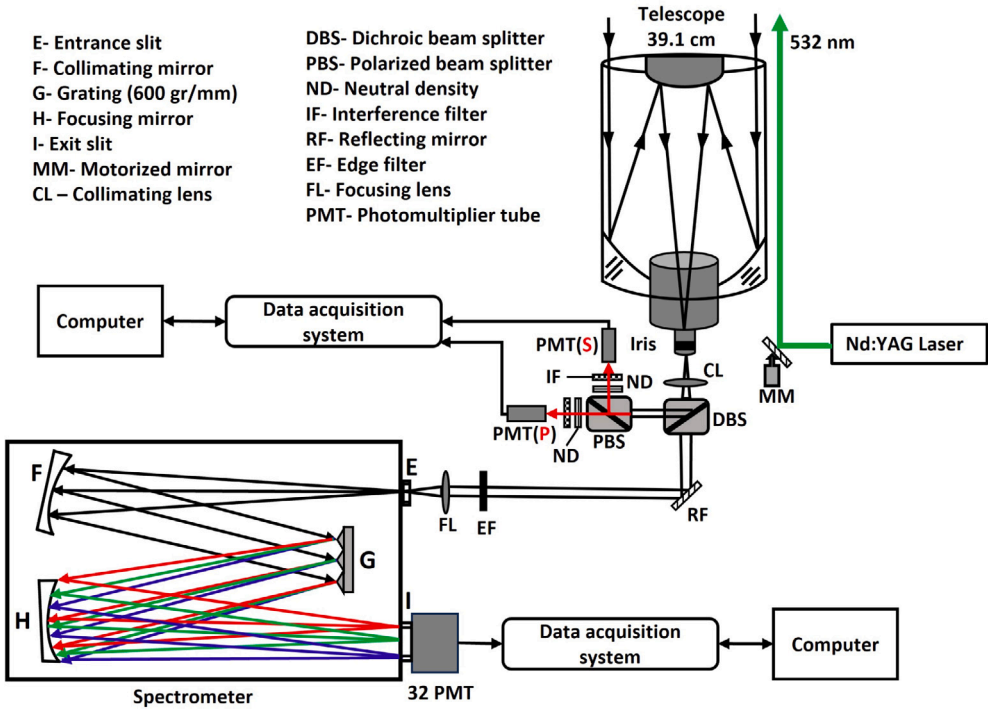

Fig. 1. Schematic diagram of the lidar system developed at the University of Hertfordshire (UH), UK.

analysis of the dust plume, Raman spectroscopic measurements were conducted simultaneously in the wavelength range of 542.9–582.5 nm. Although our instrument can, in principle, resolve the detailed chemical composition of atmospheric dust, this study focuses on identifying spectral features associated with dust layers rather than presenting detailed insights into the dust's compositional signature. This measurement example is the first step towards a more detailed analysis of the chemical signature of Saharan desert dust using spectroscopic lidar, which will be presented in follow-up contributions.

The paper is structured as follows. Section 2 briefly introduces the lidar instrumental setup, measurement location, and the methods used in this investigation. Dust detection and the description of the optical and spectral properties of dust are detailed in Section 3. Sections 4 and 5 provide the discussion and conclusions.

2. Materials and methods

2.1. Lidar system and measurement location

A multipurpose lidar system: Lidar Innovations for Technologies and Environmental Sciences (LITES) has been developed at the University of Hertfordshire, United Kingdom (51.75°N, 0.24°W, 88.5 m asl). This system is equipped with an ultra-high-energy seeded Nd:YAG laser, along with second- and third-harmonic generators. This system's design is flexible, which allows modifications for particular lidar experiments. The schematic diagram of the configuration of the lidar system used for this study is shown in Fig. 1. A more detailed description of the instrument specifications can be found in Tatarov et al. (2020), Tatarov and Müller (2021) and Tesche et al. (2018).

This lidar system emits laser pulses at the Nd:YAG fundamental wavelength of 1064 nm, along with the doubled and tripled frequency laser beams at 532 nm and 355 nm. A motorized reflecting mirror (MM) is used to guide the output beams vertically into the atmosphere to excite backscattering by particles and molecules. The backscatter signals are collected by a Schmidt-Cassegrain telescope with a diameter of 39.1 cm, followed by an iris and a collimating lens (CL). The receiving subsystem also includes a wavelength separation unit with dichroic mirrors, interference filters, and a polarization cube. The collimating lens directs the received signal to a dichroic beam splitter (DBS), which separates the elastic (Rayleigh and Mie) and inelastic (pure-rotational and rotational-vibrational) backscattered signals. The elastic signals are further separated into co-polarized (P) and cross-polarized (S) components by a polarizing beam splitter (PBS). Both components of the strong elastic signals are first attenuated by neutral density filters (ND). They are then filtered by a narrow band (1.3 nm) interference filter (IF) to suppress the background radiation before being measured by the photomultiplier tubes (PMTs). The elastic signals detected by each PMT are recorded simultaneously in both analog (AD) and photon counting (PC) modes by a two-channel Licel transient digitizer (TR20-160, Licel). The Licel digitizer features a 20 MHz analog sampling (analog to digital conversion) rate and a 250 MHz photon counting rate. Each data sampling has a bin width of 50 ns, corresponding to a range resolution of 7.5 m. A computer is used for data acquisition, system control, and real-time monitoring of the lidar operation status. Additionally, this lidar system is capable of measuring the backscattering from the Raman shifted radiation (pure-rotational and rotational-vibrational) at up to 32 different wavelengths simultaneously, along with elastic signals. The Raman and other inelastic backscattered signals, separated by the DBS, are directed to a HORIBA 1250M research spectrometer by a reflecting mirror (RF), followed by an edge filter (EF) and a focusing lens (FL). The spectrometer disperses the Raman backscattered light into their constituent wavelengths, thus allowing for the measurement of their spectra.

The dispersed spectra are then detected by the Licel SP32 multi-spectral lidar detector, equipped with a 32-multi-anode metal-channel-dynode photomultiplier (Hamamatsu H7260-20). This setup allows for the simultaneous detection across 32 spectrometer wavelengths, incorporating 32 photon counting systems. Together, these elements enable two-dimensional spectral and time-resolved data acquisition, with a time resolution of 50 ns (corresponding to a height resolution of 7.5 m). The detected signals are recorded in photon counting mode only, with a maximum count rate of 100 MHz using the Licel transient recorder.

For this measurement configuration, the spectrometer's entrance slit was set to 1000 μm, and a diffraction grating of 600 grooves/mm was

Table 1
Technical specifications of the UH lidar system used in this study.

Setup components	Technical specifications	
Transmitter	Laser type	Nd:YAG injected seeded
	Pulse energy	8 J at 1064 nm, 5 J at 532 nm, and 2.5 J at 355 nm
	Beam divergence	<0.5 mrad
	Repetition rate	10 Hz
	Linewidth	<0.003 cm^{-1}
	Pulse duration	<15 ns
Receiver	Telescope type	Schmidt-Cassegrain
	Focal length	3910 mm
	Diameter	391 mm
	FOV	0.5 mrad (adjustable)
Spectral analysis	Spectrometer	HORIBA 1250M research high-resolution spectrometer
	Focal length	1.25 m, F/9
	Accuracy	±0.15 nm
	Grating and blaze	600 g/mm with size 110 mm × 110 mm, blazed at 500 nm
Detection unit	Mie and Rayleigh scattering	PMT HV-R9880U-20 (QE ~20% at 532 nm, gain = 2×10^6)
	spectroscopic (Licel SP32-20)	Hamamatsu H7260-20 nm (32 anodes each 0.8×1 mm), spectral response: 300–920 nm
Data acquisition	Mie and Rayleigh	Licel transient recorder, 16-bit, 20 MHz A/D converters, 250 MHz photon count rate, 50 ns time (7.5 m) resolution
	Multi-anode PMT	Single photon counting system, 100 MHz count rate, 50 ns time (7.5 m) resolution

used to disperse the backscattered light. The dispersed light (time and range-resolved) was recorded by a 32-channel PMT, with each channel covering approximately 1.27 nm, providing an overall spectral range of ~40 nm from 542.9 to 582.5 nm. This range was chosen to capture dust components such as oxides, silicates, and sulfates, which exhibit prominent Raman peaks in the lower Raman shift region. Within this interval, the oxygen Raman channel at 580.0 nm was employed for lidar signal calibration and the retrieval of particle extinction and backscattering coefficients, in contrast to the more commonly used nitrogen Raman signals. Prior to measurements, spectral calibration was performed using Raman scattering calibration standards and an Ar-Hg calibration lamp. The intensity calibration of the spectroscopic part was conducted based on the wavelength-dependent efficiency of the diffraction grating and the detector's quantum efficiency, as specified by the manufacturer. The calibration was further verified with measurements from an intensity-standardized deuterium–tungsten lamp. In addition, dark current subtraction and inter-channel cross-talk corrections were applied. Table 1 provides detailed technical specifications of the Raman lidar system used in this study.

2.2. Model observations

The Copernicus Atmosphere Monitoring Service (CAMS, https://atmosphere.copernicus.eu/) provides comprehensive atmospheric composition monitoring at global and regional scales, delivering analysis and forecasts that support scientific research, environmental policy, and operational decision-making. The system monitors over 50 chemical species (e.g., O_3, NO_2, CO) and various aerosol types (desert dust, sea salt, organic matter, black carbon, sulfate, nitrate, and ammonium aerosol), along with estimates of source emissions, surface fluxes, and supplementary products. CAMS employs a physics- and chemistry-based atmospheric model that incorporates emissions, transport, chemical transformation, and deposition processes, integrating observations from Copernicus Earth observation satellites (particularly the Sentinel missions (Berger et al., 2012; Malenovský et al., 2012)) and other relevant satellite and surface measurements.

For this study, CAMS data served a dual purpose: operational planning and quantitative analysis. Initially, the CAMS European air quality forecast was used to track dust plumes (this study) and to prepare for the lidar measurements. Subsequently, for the detailed analysis, we employed the CAMS European air quality reanalysis (PM10, dust) at higher spatial (10 km × 10 km) and temporal (1 h) resolutions. This reanalysis dataset is generated through an ensemble approach that uses eleven air quality data assimilation systems across Europe, each of which operates at several vertical height levels. We selected the median ensemble product for our analysis, as ensemble products consistently demonstrate superior performance compared to individual model outputs. To complement the dust concentration data, we incorporated the Dust Aerosol Optical Depth (DAOD) product at 550 nm from the CAMS global reanalysis (EAC4: ECMWF Atmospheric Composition Reanalysis 4), which provides data at $0.75° \times 0.75°$ spatial resolution and 3-h temporal resolution. Model outputs for both dust concentration and optical depth were accessed through the Copernicus Atmosphere Data Store (https://ads.atmosphere.copernicus.eu/), operated by the European Centre for Medium-Range Weather Forecasts (ECMWF).

2.3. Satellite observations

The Visible Infrared Imaging Radiometer Suite (VIIRS) instrument is on board the joint NASA/NOAA Suomi National Polar orbiting Partnership (Suomi NPP) satellite (Jackson et al., 2013). It overpasses the equator approximately at 13:00 local time on its ascending/daytime orbit. The Suomi NPP/VIIRS Corrected Reflectance True Color product provides natural-looking images of Earth's surface and atmospheric features by combining specific wavelength bands: Red (Band I1: 600–680 nm), Green (Band M4: 545–565 nm), and Blue (Band M3: 478–498 nm). These images are particularly useful for observing land surface features, oceanic phenomena, and atmospheric conditions. The corrected reflectance imagery enhances clarity and brightness by removing gross atmospheric effects such as Rayleigh scattering from the visible bands, making them clearer than uncorrected top-of-atmosphere radiance products. The sensor resolution is 750 m for M Bands and 375 m for I Bands, with an imagery resolution of 250 m and a daily temporal resolution. For further details on these products and algorithms, see the publications by Cao et al. (2013, 2014) and Jackson et al. (2013). These images can be accessed through the open-source code application Worldview (https://worldview.earthdata.nasa.gov/) provided by NASA's Earth Observing System Data and Information System (EOSDIS). The VIIRS Deep Blue Aerosol Type layer product (`AERDB_L2_VIIRS_SNPP`) provides information related to aerosol composition over land and ocean for daytime, cloud-free, and snow-free scenes. The L2 Deep Blue Aerosol Optical Thickness data products at 550 nm are derived from specific VIIRS bands using two primary retrieval algorithms: the Deep Blue algorithm over land and the Satellite Ocean Aerosol Retrieval (SOAR) algorithm over the ocean. The sensor/algorithm resolution is 6 km at nadir, with an imagery resolution of 2 km at nadir and a daily temporal resolution. For more detailed information on these algorithms and products, we refer to Hsu et al. (2013, 2019) and Sayer et al. (2018). Although the satellite overpass time, insufficient spatial resolution, limitations of the Deep Blue algorithm, and cloud cover may present constraints in aerosol identification.

2.4. HYSPLIT back trajectory

HYSPLIT (https://www.arl.noaa.gov/hysplit/) is a comprehensive system for calculating air parcel trajectories and conducting complex simulations of the transport, dispersion, chemical transformation, and deposition of substances that are transported and dispersed through the atmosphere. The model employs a hybrid computational method that combines the Lagrangian and Eulerian approaches. The Lagrangian approach uses a moving frame of reference for advection and diffusion calculations as trajectories or air parcels move from their initial locations. In contrast, the Eulerian methodology uses a fixed three-dimensional grid to compute pollutant air concentrations. Backward trajectory analysis allows us to determine the likely origin of dust plumes and establish source-receptor relationships. A detailed description of the HYSPLIT modeling system is available in Rolph et al. (2017) and Stein et al. (2015). The accuracy of the HYSPLIT trajectory analysis depends on the quality of the input meteorological data. Inaccurate or coarse input data can lead to errors in determining dust transport pathways.

2.5. AERONET observations

The AERONET program (https://aeronet.gsfc.nasa.gov/) is a federated global network of ground-based sun photometers established by NASA in collaboration with various organizations. It provides datasets of aerosol optical, micro-physical, and radiative properties for aerosol research and characterization, validation of satellite retrievals, and synergism with other databases. Version 3 of the Aerosol Optical Depth (AOD) data is computed for three quality levels: Level 1.0 (unscreened), Level 1.5 (cloud-screened and quality-controlled), and Level 2.0 (quality-assured). Additional AOD dependent products are derived from these data-product levels. A detailed description of the AERONET datasets and their applicability can be found in Dubovik et al. (2000), Dubovik and King (2000), Eck et al. (2014), and Giles et al. (2019). The AOD and Ångström Exponent (AE) parameters, which describe the optical thickness and size of particles (in qualitative terms), respectively, were used to validate the lidar measurements in this study. The nearest AERONET station, Bayfordbury observatory (51.776°N, 0.096°W), operated by the University of Hertfordshire, is located 75 m above sea level and approximately 10 km northeast of our lidar laboratory. Due to the unavailability of cloud-screened data at the Bayfordbury observatory, two additional AERONET stations were considered: Lille, France (50.61°N, 3.14°E, 60 m asl), located approximately 267 km southeast, and the University of Manchester (UoM), UK (53.47°N, 2.23°W, 94 m asl), located about 232 km northwest of the lidar site. These stations were selected based on the availability of at least Level 1.5 data and their location under the pathway of the dust plume.

2.6. Lidar measurements and dust characterization

For this observation, we employed a linearly polarized laser with a wavelength of 532 nm and a pulse energy of 1.5 J at 10 Hz. Each lidar profile was obtained by averaging 600 laser shots per minute, with a vertical resolution of 7.5 m. The system provides full overlap at about 250–350 m from the lidar for the elastic signals and ~2 km for the spectroscopic signals, depending on the system settings. This difference arises because the elastic signals are collected through the wide/full field of view (FOV) of the telescope and directed to the detector after spectral separation, allowing overlap to be reached at lower altitudes. In contrast, the Raman signals pass through a spectrometer with a narrow entrance slit, which restricts the effective FOV and shifts the full overlap to higher altitudes. The extended daylight hours on the measurement day resulted in a poor signal-to-noise ratio (SNR) for the Raman signals. To increase the SNR, elastic and inelastic signals were smoothed over 600 m using a gliding signal-averaging window. Clouds were persistent between 6–11 km above the dust plume during the measurement. Later, thick, low-level clouds appeared, and measurements were stopped because of the onset of drizzle.

2.6.1. Extinction and backscattering coefficients

The received signals result from the attenuation and backscattering generated by air molecules (Rayleigh scattering) and aerosol particles, which are always present in the atmosphere. When dust or other particulates are introduced, they increase the extinction and backscattering of the laser pulses. By comparing the measured signal to the expected signal from a clean (particle-free) atmospheric background, the presence of these particles can be identified. However, to retrieve the optical parameters, such as extinction and backscattering coefficients, from lidar measurements, the received signals must be processed. The algorithms for data processing differ for different phenomena: elastic scattering, Raman scattering, and fluorescence. A detailed description of these algorithms is presented by Ansmann et al. (1990, 1992), Fernald (1984), Klett (1981), and Sugimoto et al. (2012). We employed the Raman lidar technique to independently retrieve the particle extinction coefficients by using both elastic and inelastic (Raman) return signals. While nitrogen Raman signals are commonly used for this purpose because of their higher concentration (78% of the air molecules), in this study, we utilized oxygen (21% of air molecules) Raman signals at 580.0 nm (with 532 nm pumping) to derive the particle extinction $\alpha_{\mathrm{par}}(z)$ and backscattering coefficients $\beta_{\mathrm{par}}(z)$. This choice was driven by the spectral coverage limitation of our spectrometer (~40 nm) and our focus on observing mineral components, which exhibit relatively lower characteristic Raman shifts. The relatively high laser energy enabled us to achieve a reasonable SNR of the oxygen Raman signals, even at low oxygen concentrations. These parameters were computed for two selected time periods. The particle extinction-to-backscatter (lidar) ratio $L_{\mathrm{par}}(z)$ and the integrated extinction coefficient, i.e., the aerosol optical depth, can be readily derived. These parameters can be used to infer the total particle load in the atmospheric column and their vertical distribution, and they help distinguish between different particle types. Lidar signals were calibrated and validated with the molecular profiles (α_{m} and β_{m}) derived from atmospheric density profiles calculated from radiosonde pressure and temperature measurements. These radiosonde measurements were obtained at the nearest station, i.e., in Nottingham, UK, and were provided by the National Centers for Environmental Information (NCEI: https://www.ncei.noaa.gov/data/integrated-global-radiosonde-archive/access/data-por/). Finally, AOD at a wavelength λ is given by

$$\mathrm{AOD}(\lambda) = \int_{z_1}^{z_2} \alpha(z,\lambda)\,\mathrm{d}z \tag{1}$$

Here, z_1 and z_2 represent the lower and upper limits of the atmospheric column (altitude range) for which the optical depth is to be computed.

2.6.2. Lidar ratio

The lidar ratio, defined as the ratio of the aerosol extinction coefficient (α) to the aerosol backscattering coefficient (β), is a fundamental parameter in atmospheric lidar remote sensing:

$$L_{\mathrm{par}}(z) = \frac{\alpha_{\mathrm{par}}(z)}{\beta_{\mathrm{par}}(z)} \tag{2}$$

It serves as an indicator of the aerosol type. Large L_{par} values are associated with highly light-absorbing particles, while low L_{par} values are indicative of particles that present greater scattering. The lidar ratio varies significantly depending on the type of aerosol, its size distribution, refractive index, and the wavelength of the incident light (Ansmann and Müller, 2005).

2.6.3. Particle depolarization ratio

The presence of dust predicted by model analysis can be confirmed by lidar depolarization measurements. The depolarization ratio, which measures the change in the polarization of backscattered light, indicates the presence of non-spherical or irregularly shaped particles. Lidar depolarization measurements allow us to identify distinct

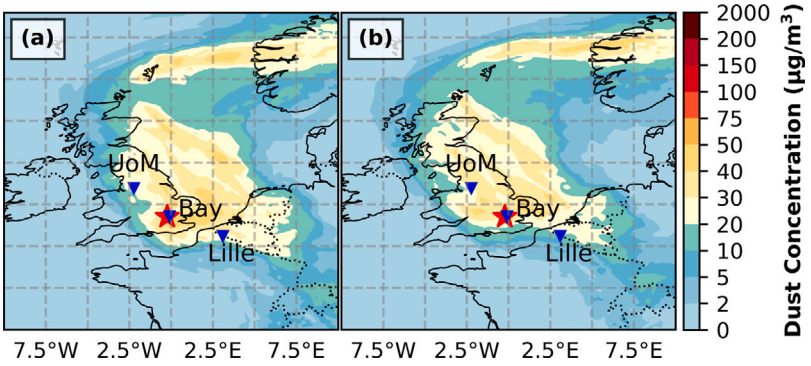

Fig. 2. CAMS European air quality reanalyses (ensemble median) showing dust concentration at 3 km altitude above the surface during the Saharan dust transport episode on 1 May 2024. Panel (a) displays conditions at 19:00 UTC, when the dust plume was positioned over the lidar observation site, while panel (b) shows the conditions at 23:00 UTC, when the plume had moved northwestward, placing the observation site on the trailing edge as it approached the UoM AERONET station. The lidar location is marked with a red star, and the three AERONET stations are shown as blue triangles.

types of atmospheric particles, e.g., low-depolarizing urban aerosols, high-depolarizing dust aerosols, and ice clouds.

It is convenient to calculate the linear volume depolarization ratio (δ_v) as a first approximation of the particle linear depolarization ratio (δ_p), because δ_v can be directly derived from the co-polarized ($P_\parallel$) and cross-polarized ($P_\perp$) signals, along with the calibration factor (C). The δ_v is a measure of the overall properties of the atmospheric volume, comprising a mixture of molecules and particles. The calibration factor accounts for the transmission of all optics and filters, as well as the electronic amplification of the PMTs and preamplifiers (channel gain ratio). Failure to correctly complete this step can lead to systematic errors with a substantial impact. Addressing instrumental effects on depolarization is crucial (Bravo-Aranda et al., 2016; Belegante et al., 2018). A comprehensive investigation of the dependence of lidar signals on polarization parameters is described in Freudenthaler et al. (2009) and Freudenthaler (2016).

$$\delta_v = C\left(\frac{P_\perp}{P_\parallel}\right) \tag{3}$$

The determination of the particle linear depolarization ratio δ_p requires a more complex procedure that corrects for the influence of air molecules and defines an intrinsic property of the particles. It can be calculated according to Biele et al. (2000) and Freudenthaler et al. (2009):

$$\delta_p = \frac{(1+\delta_m)\,\delta_v\,R - (1+\delta_v)\,\delta_m}{(1+\delta_m)\,R - (1+\delta_v)} \tag{4}$$

The backscatter ratio R is defined as:

$$R = 1 + \frac{\beta_{par}}{\beta_m} \tag{5}$$

The molecular linear depolarization ratio δ_m can be computed using the methods described by Behrendt and Nakamura (2002).

2.6.4. Spectroscopic observation

In addition to the traditional lidar observations, this study also employs a spectroscopic lidar system that is capable of measuring detailed atmospheric aerosol composition through spectrally resolved backscatter signals. The system enables discrimination between different aerosol types and atmospheric constituents based on their distinctive molecular signatures, including both inelastic scattering phenomena and fluorescence emissions from various atmospheric components. The lidar system incorporates a high-resolution spectrometer equipped with a 32-channel PMT. Each channel is precisely tuned to capture specific Raman-shifted wavelengths, allowing for comprehensive spectral analysis of the atmospheric return signals. This multi-channel approach enables the simultaneous detection of various aerosol components and their optical properties. The received power for channel i at range r is given by:

$$P_{Ri}(r,\lambda_L,\lambda_{Ri}) = P_L\frac{C\times G(r)}{r^2}\beta_{Ri}(r,\lambda_L,\lambda_{Ri}) \times \exp\left[-\int_0^r\left[\alpha_p(z,\lambda_L)+\alpha_m(z,\lambda_L)+\alpha_p(z,\lambda_{Ri})+\alpha_m(z,\lambda_{Ri})\right]dz\right] \tag{6}$$

where $i = 1, 2, \ldots, 32$ is the channel index, P_L and λ_L denote the laser power and wavelength, G(r) is the geometrical form factor of the transmitter/receiver system, C is a constant that includes all range-independent parameters, $\beta_{Ri}(r,\lambda_L,\lambda_{Ri})$ is the Raman backscatter coefficient, and α_p and α_m represent the particle and molecular extinction coefficients, respectively.

As a reference, for atmospheric molecules such as nitrogen or oxygen, the Raman lidar equation (Ansmann et al., 1990) is:

$$P_m(r,\lambda_L,\lambda_m) = P_L\frac{C\times G(r)}{r^2}\beta_m(r,\lambda_L,\lambda_m) \times \exp\left[-\int_0^r\left[\alpha_p(z,\lambda_L)+\alpha_m(z,\lambda_L)+\alpha_p(z,\lambda_m)+\alpha_m(z,\lambda_m)\right]dz\right] \tag{7}$$

The Raman backscatter coefficient for a particular chemical compound is determined as:

$$\beta_{Ri}(r,\lambda_L,\lambda_{Ri}) = \xi(r)\,\frac{P_{Ri}(r,\lambda_L,\lambda_{Ri})}{P_m(r,\lambda_L,\lambda_m)}\times\beta_m(r,\lambda_L,\lambda_m) \times \exp\left[-\int_0^r\left[\alpha_p(z,\lambda_{Ri})+\alpha_m(z,\lambda_{Ri})-\alpha_p(z,\lambda_m)-\alpha_m(z,\lambda_m)\right]dz\right] \tag{8}$$

In the above equation, the wavelength dependence of extinction in the exponent can be replaced by the term $\eta(r,\lambda_{Ri},\lambda_m)$. To solve this equation, the ratio of the system parameters of the Raman and molecular channels ξ(r), molecular backscattering and extinction profiles, as well as particle extinction profiles at the respective Raman wavelength must be known. Atmospheric molecular scattering profiles can be obtained from model data or from the temperature and pressure profiles derived from standard meteorological measurements. The aerosol extinction profile at the Raman wavelength can be obtained from the aerosol extinction profile at the laser wavelength by assuming a power-law wavelength dependence (Ansmann et al., 1990). The relationship between Raman backscatter coefficients β_{Ri}, Raman backscatter differential cross-section $\frac{d\sigma_i(\lambda_L,\lambda_{Ri},\pi)}{d\Omega}$, and the number density of a particular chemical component N_i can be expressed as follows, where $d\Omega$ denotes

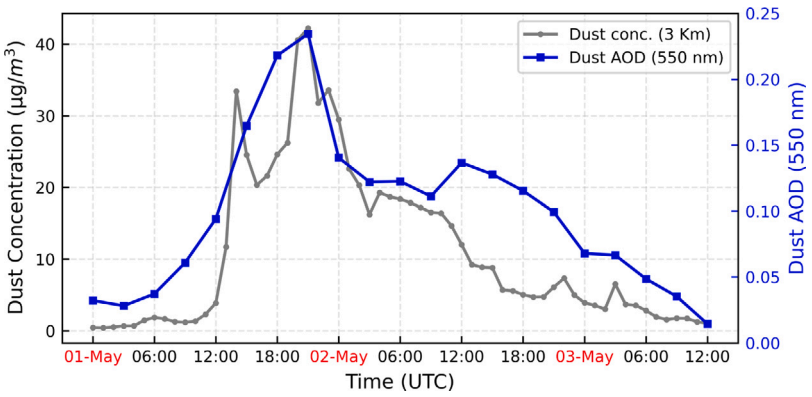

Fig. 3. Time series from 1–3 May 2024 showing the dust concentration at 3 km altitude from the CAMS European air quality reanalysis (10 km × 10 km) and DAOD at 550 nm from the CAMS global reanalysis (EAC4) (0.75° × 0.75°) over the lidar site.

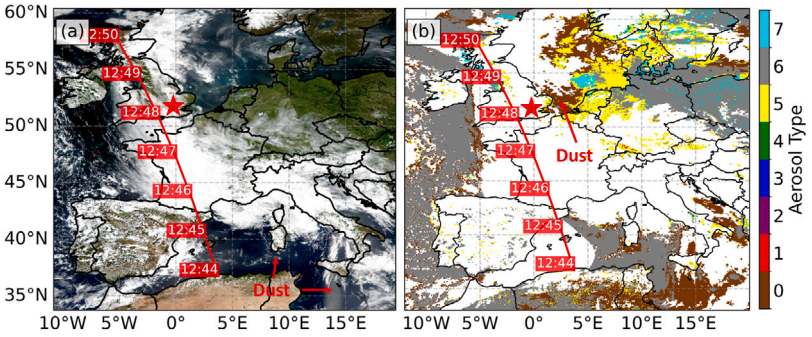

Fig. 4. (a) Corrected true color reflectance image captured on 1 May 2024 by the VIIRS instrument aboard the NASA/NOAA Suomi NPP satellite. (b) Aerosol compositions are derived using the Deep Blue algorithm from the same set of data collected by the satellite sensors. The aerosol types are classified as follows: 0 = Dust, 1 = Smoke, 2 = High altitude smoke, 3 = Pyrocumulonimbus clouds, 4 = Non-smoke fine mode, 5 = Mixed, 6 = Background, 7 = Fine-mode dominated. The observation site is marked with a red star. The times indicate the overpass times of the satellite in UTC.

the solid angle in steradians over which the scattering is measured.

$$\beta_{Ri}(r, \lambda_L, \lambda_{Ri}) = N_i(r) \frac{d\sigma_i(\lambda_L, \lambda_{Ri}, \pi)}{d\Omega} \quad (9)$$

With the known differential cross-section of atmospheric gasses and solid (as well as liquid) aerosol components, the number density and therefore their mass concentration (N_i × molecular mass) can be estimated using the above expression. An example of how profiles of mass concentration can be calculated is given by Müller et al. (2010) and Tatarov et al. (2011).

Here we present an example of the spectrally resolved lidar signals obtained during the Saharan dust event on 1 May 2024 over Hatfield, UK. Unlike the single-PMT lidar measurements depicted in Fig. 7(a), the 32-channel spectroscopic system used here offers continuous, gap-free spectral data. For the spectral analysis, two distinct time periods were selected: 20:30–21:20 UTC and 23:15–23:59 UTC. These intervals correspond to low-level, cloud-free conditions and post-sunset periods, minimizing solar background interference and enhancing the signal-to-noise ratio of the spectroscopic measurements. Additionally, we compared and analyzed the spectral signature of the low-level cloud (22:00–23:00 UTC) and the underlying dust layer. Unlike the elastic channel, the Raman (inelastic) channels acquire a full overlap at a higher range (~2 km), depending on the spectrometer entrance slit size. Unfortunately, reliable overlap correction functions for the Raman channels are not available for this system configuration. Nevertheless, we are able to present spectrometer-derived results based on the ratios of the inelastic channels, independent of the overlap effect.

3. Results

3.1. Model output and satellite observations

The CAMS European air quality reanalysis data presented in Fig. 2 captures a Saharan dust transport episode that occurred over the UK on 1–2 May 2024. This analysis reveals the temporal evolution (between 19:00 and 23:00 UTC) and spatial dynamics of elevated dust concentrations at the 3 km altitude level. At 19:00 UTC, the dust plume appears to be centered over the lidar site. At the same time, the Lille AERONET station seems to be located beneath the departing edge of the plume. By 23:00 UTC, the lidar site was located under the trailing edge of the plume as it moved northwest toward the UoM AERONET station.

Fig. 3 presents complementary time series data (1–3 May 2024) from two CAMS datasets: dust concentration from the European air quality reanalysis (10 km × 10 km spatial resolution) and dust aerosol optical depth at 550 nm from the global reanalysis data, which has a spatial resolution of 0.75° × 0.75°. Both model outputs confirm the arrival of the dust plume over the study location during the afternoon of 1 May 2024. The European reanalysis indicates peak dust concentrations of approximately 40 μg/m^3 at 3 km altitude above ground level, between 19:00 and 21:00 UTC. Simultaneously, the global reanalysis shows that DAOD at 550 nm reaches a maximum value of 0.24 during this period, which corresponds to moderate dust loading conditions. Consequently, the lidar measurement was scheduled to capture this peak period of dust advection over the UK. The slight discrepancies between dust concentration and optical depth values can be attributed to fundamental differences between the two datasets, including their distinct

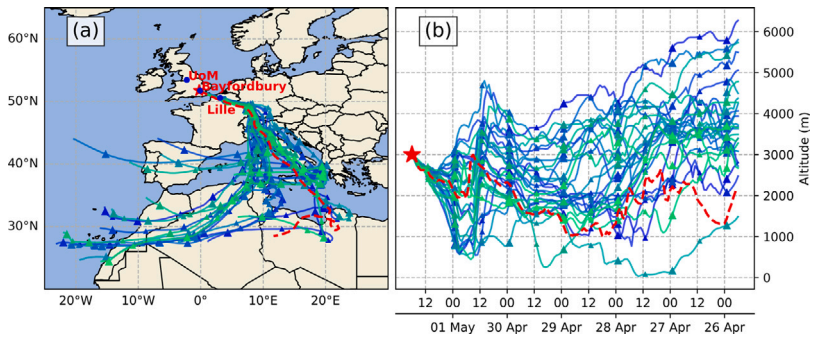

Fig. 5. (a) HYSPLIT 6-days ensemble trajectories starting backward at 19:00 UTC on 1 May at 3000 m above ground level. (b) Dispersion paths at various altitudes over the 6 days. The AERONET stations used in this study: Lille, Bayfordbury and UoM are shown as blue dots. Additional single trajectories are shown as red dashed lines.

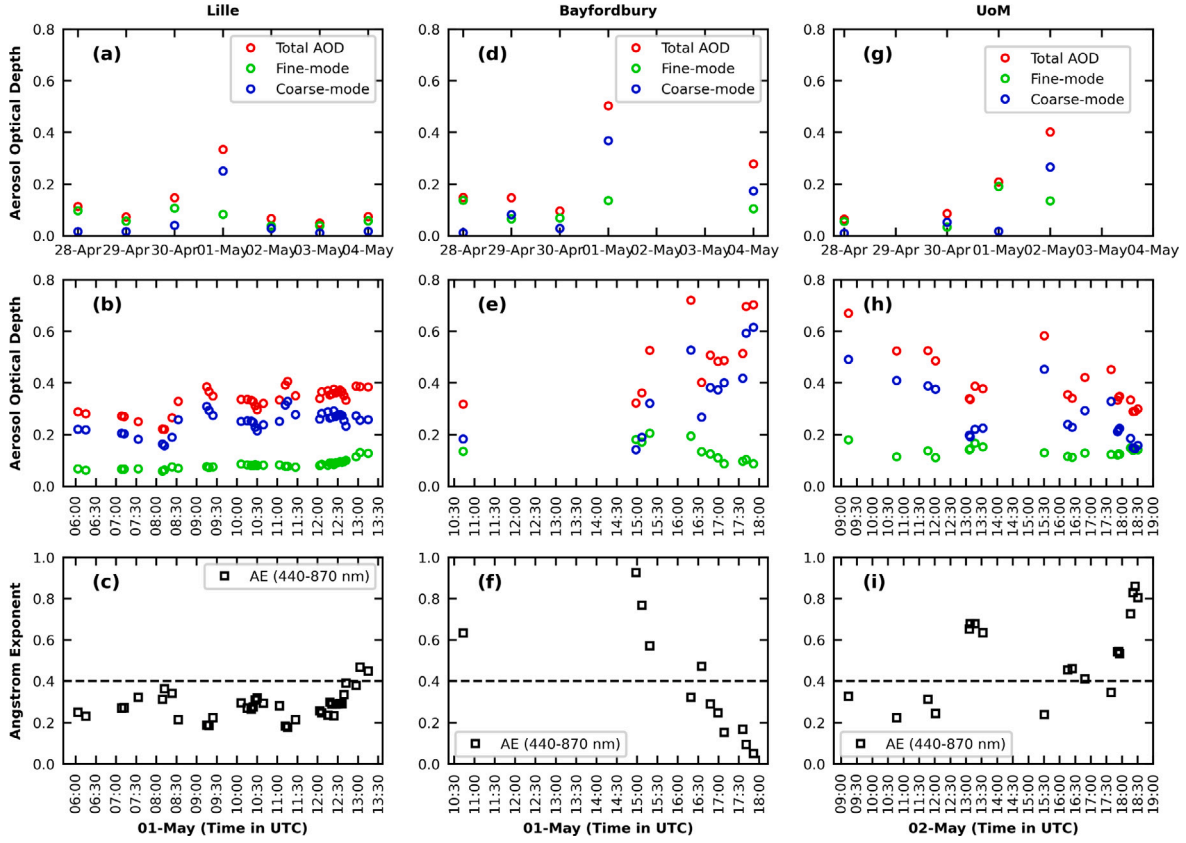

Fig. 6. Daily mean AOD (top row) and diurnal AOD (middle row) at 500 nm for total (red), fine-mode (green), and coarse-mode (blue) aerosols on 1 May at Bayfordbury and Lille, and on 2 May at UoM. The bottom row shows corresponding Ångström exponent values at 440–870 nm. Data are presented for the Lille (a–c), Bayfordbury (d–f), and UoM (g–i) AERONET stations. The horizontal dashed black line indicates the AE threshold value of 0.4.

spatial resolutions (10 km versus ~80 km grid size) and inherent model characteristics.

Fig. 4 shows the path and overpass time of the Suomi NPP satellite on its ascending/daytime orbit.

The satellite passed over Western Europe approximately 120 km west of the lidar location at around 12:48 UTC on 1 May 2024. Fig. 4(a) presents the corrected true color reflectance imagery captured by VIIRS (aboard Suomi) on that day. In the true color satellite imagery, plumes of atmospheric dust are visible as hazy patches over the western part of the Mediterranean Sea, i.e., the Tyrrhenian and Balearic Seas. However, due to extensive cloud cover, it is difficult to identify the dust around the observation location and in most parts of the imagery. Fig. 4(b) shows aerosol types derived using the Deep Blue algorithm. The cloud-free scene is dominated by dust and mixed types of aerosols over the North Sea to the east of the UK. The west of Europe was under cloud cover, preventing the retrieval of information on aerosol types. At 12:48 UTC, dust and mixed aerosols were visible over the coast of southeastern England, closer to our lidar site. The observation location is marked with a red star in both images.

3.2. HYSPLIT back trajectory

To investigate the source and transport pathway of the observed Saharan dust plume, HYSPLIT backward trajectories were calculated. Fig. 5 illustrates an ensemble of 6-day backward trajectories, starting at 19:00 UTC on 1 May 2024, at an altitude of 3 km. These trajectories

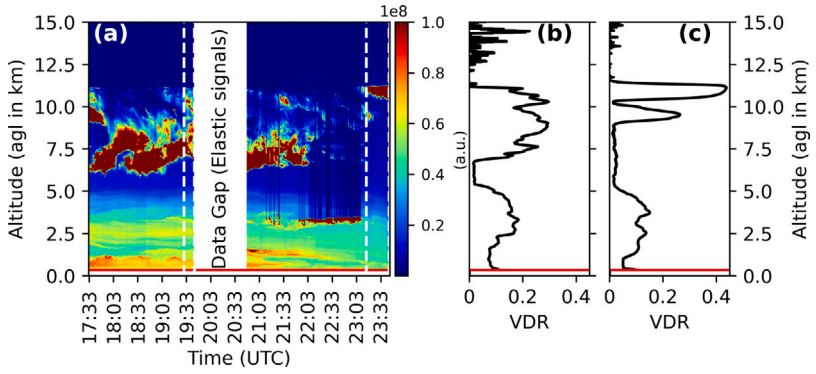

Fig. 7. (a) Spatiotemporal variation of range-corrected lidar signals at 532 nm on 1 May 2024. Panels (b) and (c) show average volume depolarization ratio (VDR) profiles between 19:30 to 19:43 UTC and 23:15 to 23:44 UTC, respectively (marked by white dashed lines), which are used to characterize the dust plume in this study. The red horizontal line indicates the full-overlap altitude for the elastic channels.

provide critical insights into the long-range transport of the dust plume and its interaction with other atmospheric components during transit. The trajectories reveal that the air mass, which originated on April 26 from Northwest Africa, crossed the Mediterranean Sea and traveled across Italy before taking a course toward the UK, where it arrived on 1 May, as shown in Fig. 5(a). The trajectories below 2 km indicate that vertical mixing of the dust plume with anthropogenic pollutants may have taken place during the transport, as illustrated in Fig. 5(b). The results of our lidar observations (see Sections 3.4 and 4) show that the lower part of the dust plume may have been mixed with urban pollution.

3.3. AERONET observations

Fig. 6 presents AERONET sun photometer observations from Lille, Bayfordbury, and the University of Manchester. These ground-based measurements provide independent information on the dust plume's arrival, intensity, and evolution, complementing the lidar-derived vertical profiles. The analysis focuses on AOD, along with total, fine mode, and coarse mode aerosols at 500 nm, and the Ångström exponent over the 440−870 nm wavelength range. These two parameters, widely used in aerosol characterization, allow for the identification of dust plumes based on their coarse-mode particle dominance. Following the methodology of Tesche et al. (2009), an AE threshold of ≤0.4 is used to indicate the presence of Saharan dust. This threshold value is based on lidar and sun photometer observations taken in Northwest Africa during the Saharan Mineral Dust Experiment (SAMUM) 2006.

The Lille AERONET site, located approximately 260 km southeast of the primary lidar observation location, was the first to detect the arrival of the dust event (Fig. 6a–c). Compared to the preceding and following days, the highest daily AOD at 500 nm was observed on 1 May 2024, with a total AOD of 0.33. On this day, the coarse-mode AOD contributed 0.25 (76%) and the fine-mode AOD contributed 0.08 (24%) to the total AOD, indicating that the aerosol loading was predominantly from coarse particles. The temporal evolution on 1 May shows a notable increase in both total and coarse-mode AOD after 08:00 UTC, accompanied by a concurrent decrease in AE, suggesting the advection of coarse-mode particles, which is typically associated with mineral dust. Notably, the diurnal variations of total AOD and coarse-mode AOD follow a similar pattern, which indicates the dominance of coarse particles during the early phase of the event. Around 12:00 UTC, AE values began to increase above 0.5, accompanied by a slight increase in fine-mode AOD and a slight decrease in coarse-mode AOD. This change, however, should be interpreted with caution. While it may suggest the arrival of a plume containing both transported dust and local anthropogenic aerosols, the observed increase in fine-mode AOD could also be the result of local contributions within the boundary layer. Therefore, attributing this variation solely to the transported dust plume is not justified.

At Bayfordbury (Fig. 6d–f), the daily average AOD at 500 nm peaked at 0.50 on 1 May, based on Level 1.0 data. On this day, the coarse-mode AOD was 0.37 (74%), and the fine-mode AOD was 0.13 (26%). Compared to Lille, where the coarse-mode contribution was 76%, this slight decrease in the coarse-mode fraction and slight increase in the fine-mode contribution suggest a modest shift toward finer particles as the plume moved northwest. However, it is important to note that these measurements are derived from Level 1.0 data, which is not fully quality-assured. Moreover, the apparent increase in the fine-mode fraction should not be directly interpreted as a modification of the dust size distribution during transport, since local sources of fine aerosols in the boundary layer (e.g., urban or industrial emissions) could also contribute to the observed signals. Beginning around 15:00 UTC, a comparably strong upward trend in total AOD was observed, which coincided with a marked decrease in Ångström exponent values. By 17:00 UTC, AE values dropped to between 0.2 and 0.05, while AOD rose to between 0.4 and 0.7 at 500 nm. These changes indicate the arrival of the dust plume at Bayfordbury, with the low AE values confirming the dominance of coarse-mode particles during the peak of the event. This is further supported by a simultaneous drop in fine-mode AOD and an increase in coarse-mode AOD, which corroborates the interpretation that aerosol loading was primarily driven by transported mineral dust.

At the University of Manchester site, located approximately 235 km northwest of Bayfordbury, the highest daily average AOD at 500 nm was recorded on May 2, reaching 0.40 (Fig. 6g–i). On this day, the coarse-mode AOD was 0.27 (67%) and the fine-mode AOD was 0.13 (33%). Compared to Lille, where the total AOD was 0.33 with a fine-mode contribution of 24%, the data from UoM show a moderate increase in total AOD after one day of transport, along with an increase in the fine-mode fraction (from 24% to 33%) and a corresponding decrease in the coarse-mode fraction (from 76% to 67%). It is important to highlight that this apparent shift should not be considered as direct evidence of mixing between dust and fine-mode aerosols during transport. Fine-mode particles are often concentrated in the boundary layer and may arise from local or regional emissions rather than being mixed into the long-range transported dust plume itself. Thus, the observed increase in fine-mode fraction at UoM could reflect the superposition of transported dust with locally emitted aerosols rather than a modification of the dust size distribution along the transport pathway. Between 09:00 and 13:00 UTC on May 2, a gradual decline in total AOD was observed alongside a rise in the Ångström exponent, which indicates a reduction in coarse-mode particles and a transition toward finer aerosol dominance. A secondary AOD peak occurred around 15:30 UTC, reaching 0.60, along with a drop in AE to 0.20, which indicates a renewed intrusion of coarse-mode dust

within a mixed aerosol environment. Again, the fine-mode contribution during this phase should be considered with caution, since local aerosol sources within the boundary layer could play a significant role.

Throughout the day, the fine-mode AOD remained relatively stable, while fluctuations in total AOD and AE were primarily driven by variations in coarse-mode aerosol loading. By 18:00 UTC, AE values increased to between 0.5 and 0.8, with a decline in both total and coarse-mode AOD, indicating that the dust plume had moved away from the observation site.

3.4. Lidar observations

Fig. 7(a) presents a time-height display of the range-corrected lidar signal acquired between 17:33 and 23:44 UTC on 1 May 2024. Panels (b) and (c) illustrate the volume linear depolarization ratio at 532 nm, which serves as a key parameter for distinguishing between spherical and non-spherical particles and for the identification of different aerosol types.

The intensity of the returned signal is proportional to the aerosol and cloud backscatter, providing a qualitative overview of the atmospheric structure during the observation period. The lidar measurement reveals the presence of a distinct aerosol layer located between 2 and 5 km altitude, above the planetary boundary layer (PBL). The higher backscatter within this layer suggests particulate loading. Above this aerosol layer, persistent high-altitude clouds were observed between 6 and 12 km throughout the measurement period. A relatively clear, aerosol-free region is evident between the dust layer and the high-altitude clouds, indicating a separation of these atmospheric features. Between 21:00 and 23:00 UTC, low-level dense clouds were observed within the aerosol layer at an altitude of 3–4 km. These clouds strongly attenuated the lidar signals. By approximately 00:12 UTC on 2 May 2024, low-level clouds appeared below 1 km, and measurements were subsequently stopped due to drizzle.

The subsequent analysis focuses on quantifying the optical properties (extinction coefficient, backscattering coefficient, lidar ratio, and particle linear depolarization ratio) of the observed dust layer. We explored the different time windows under conditions of cloud-freeness and enough SNR (night-time) of the oxygen Raman channel to estimate the extinction and backscattering coefficients. We found that the two time windows, 19:30–19:43 and 23:15–23:44 UTC fulfilled these conditions, and the height range between 5.5 and 6 km was relatively clear of particles and cloud free. Thus, we could use this height range to calibrate the lidar signal profiles and separate particles from molecules. We note that we would have preferred to use the height range above 12 km, but limitations due to poor SNR did not allow for this more robust approach to lidar signal calibration.

We calculated the backscatter coefficients β_{par}, the extinction coefficients α_{par}, the lidar ratios L_{par}, and the particle linear depolarization ratios δ_{par} at 532 nm. Fig. 8 illustrates the mean profiles (thick solid lines) of these optical properties for the two selected time intervals. The mean profiles of α_{par}, β_{par}, L_{par}, and δ_{par} are presented for altitudes between 2.0–5.0 km above ground level, due to the poor SNR of the oxygen Raman signals above ~5.0 km and incomplete overlap below 2 km. The horizontal bars denote the associated standard error of the mean (SEM). For the lidar ratio, the mean values (black squares) for layers at different heights are shown; each value has been calculated as the mean for the layer of 500 m between 2 and 5 km.

Fig. 8 presents the vertical profiles of aerosol optical properties derived from lidar measurements at 532 nm during two observation periods: (a–d) from 19:30 to 19:43 UTC and (e–h) from 23:15 to 23:44 UTC. The panels illustrate the extinction coefficients (a, e), backscattering coefficients (b, f), lidar ratios (c, g), and particle linear depolarization ratios (d, h).

During the first observation period (19:30–19:43 UTC), the extinction coefficient (Fig. 8a) peaked at ~130 Mm^{-1} around 3 km altitude, with an integrated AOD (2–5 km) of 0.26 at 532 nm, indicating moderate aerosol loading. The corresponding backscatter profile (Fig. 8b) shows similar peaks, confirming the dust plume structure. The lidar ratios for each 500 m altitude interval (Fig. 8c) yielded an overall layer-averaged value of 53 ± 14 sr, which is consistent with dust aerosols. The linear particle depolarization ratio profile (Fig. 8d) provides further evidence of dust dominance but also reveals vertical variability within the 2–5 km layer. An overall layer-mean depolarization value of 0.25 ± 0.02 was observed, consistent with dust-dominated conditions. However, lower depolarization values (0.22 ± 0.02) were found around 2–3 km, which may suggest the influence of more spherical particles, possibly from local boundary layer sources (such as urban and marine aerosols) that have been entrained into or co-located with the dust layer. At higher altitudes (3–5 km), depolarization values increased to (0.27 ± 0.02), consistent with the dominance of non-spherical dust particles and the reduced influence of local sources.

During the second observation period (23:15–23:44 UTC), the extinction coefficient values were slightly lower, peaking at ~100 Mm^{-1} at ~3 km altitude, with an AOD (2–5 km) of 0.19, showing temporal evolution and a decrease in aerosol loading over the approximately 4-h period. The lidar ratios during this time period ranged from 40 ± 5 sr to 56 ± 22 sr (mean: 51 ± 11 sr), remaining consistent with the typical range for Saharan dust (40–60 sr) reported in previous studies (Papayannis et al., 2008; Soupiona et al., 2020; Haarig et al., 2022; Ansmann et al., 2003; Mattis et al., 2002). Examining the particle linear depolarization ratio profile (Fig. 8h) reveals increased complexity in the vertical structure compared to the earlier period. Lower particle linear depolarization values of 0.20 ± 0.01 were observed between 2–3 km, which is consistent with the continued possible mixing of dust with local aerosols or the presence of more spherical particles. A distinct minimum in particle linear depolarization was observed between 3–4 km, coinciding with the formation of liquid clouds within the aerosol layer. This change likely reflects the hygroscopic growth of coated dust particles (e.g., dust mixed with soluble material) under high relative humidity, which likely contributed to particle sphericity and thereby reduced the depolarization signal through the hygroscopic growth process. However, the particle linear depolarization value increases substantially to 0.28 ± 0.01 between 4–5 km, indicating a clear return to a dust-dominated aerosol population at higher altitudes, where cloud processing effects are minimal.

3.4.1. Spectroscopic measurements

Fig. 9 displays the spectrally resolved (32 channels: 542.9 nm to 582.5 nm) and vertically resolved profiles of lidar signals averaged over two selected time intervals: 20:30–21:20 UTC and 23:15–23:59 UTC. These profiles allow us to investigate both the temporal and vertical variations of the dust composition in terms of Raman lines that may be specific to particular components in this dust plume. We emphasize that this work is just the first step in more detailed investigations of the chemical signatures of mineral dust using our spectroscopic lidar. We will present a more detailed study in a future contribution.

For each time period, we extracted the averaged spectra for the following altitude ranges: 0.5–1 km, 1–2 km, 2–3 km, an integrated dust layer (0.5–3 km), as well as layers between 3–4 km and 4–5 km. All the spectra are normalized to the oxygen Raman signal. A distinct spectral peak was consistently observed around 571.0 ± 1.3 nm (corresponding to Raman shifts of 1284 ± 40 cm^{-1}) across all profiles up to 3–4 km altitude in both time periods. A comparable Raman feature at ~1350 cm^{-1} was observed in laboratory Raman measurements of desert sand (532 nm excitation; Fig. 10e). However, direct equivalence cannot be confirmed due to the large difference in spectral resolution between laboratory (0.05 nm corresponding to 1–2 cm^{-1}) and lidar (1.3 nm corresponding to 40 cm^{-1} at 532 nm excitation) measurements and the fact that we have no independent information on the type (i.e., chemical composition) of the desert dust we observed. Above 4 km, this spectral feature becomes indistinct, likely due to the weaker Raman backscatter signals and the thinning of the dust layer (see Fig. 7a). It is

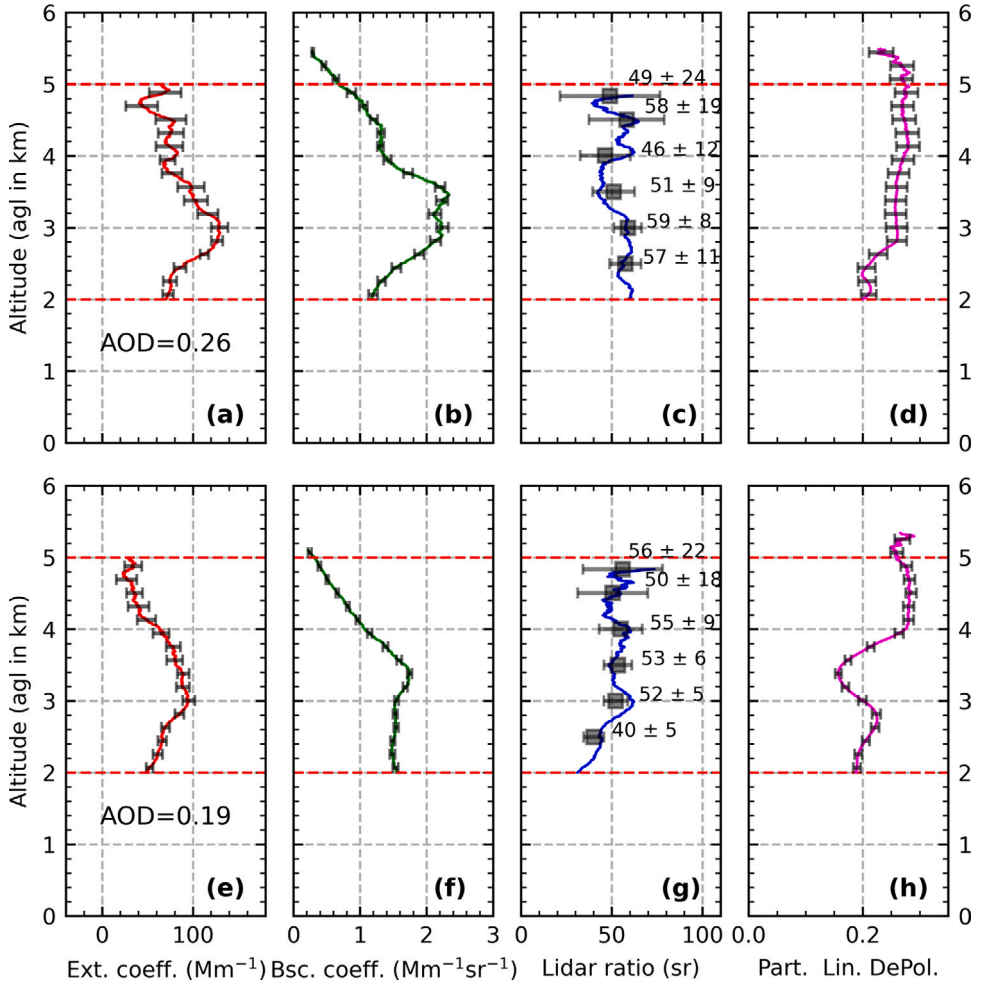

Fig. 8. Dust optical properties at 532 nm measured with Raman lidar between (a–d) 19:30 to 19:43 UTC, and (e–h) 23:15 to 23:44 UTC on 1 May 2024. The uncertainties in terms of standard deviations of the parameters are presented by the error bars. The altitude range of 2–5 km between the dashed red lines represents the region of interest where the dust layer is present.

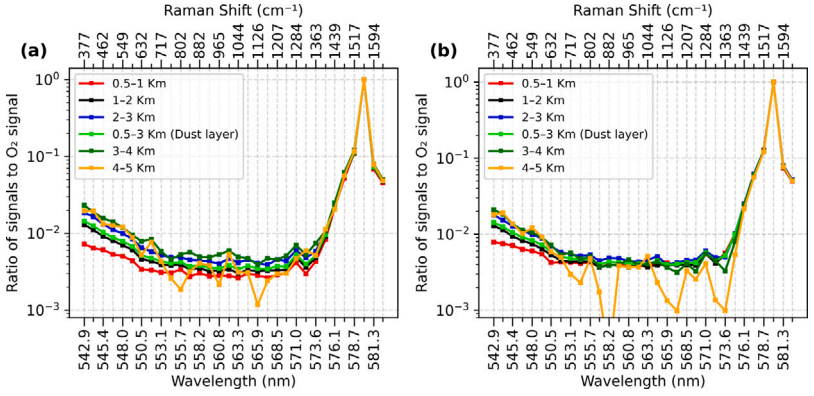

Fig. 9. Spectrally resolved and height resolved lidar signals of the Saharan dust event observed over Hatfield, UK on 1 May 2024 (a) Spectral profiles averaged from 20:30–21:20 UTC; (b) profiles averaged from 23:15–23:59 UTC. The bottom x-axes show all 32 detection channels spanning 542.9–582.5 nm, while all range-resolved spectra are normalized to the oxygen Raman channel at 580.0 nm. The top x-axes show the values of Raman shifts in terms of wavenumber.

noteworthy that the intensity of the peak at 571.0 nm is approximately 100 times lower than that of the atmospheric oxygen Raman peak observed at 580.0 ± 1.3 nm, recorded simultaneously under identical observational conditions. This relative intensity difference underscores the low number density or concentration of mineral dust compared to molecular species like oxygen, yet its persistent detection across the dust layer confirms its significance as a spectral fingerprint.

In addition to the 571.0 nm peak, higher signal intensities were observed in the shorter wavelength channels, specifically from 542.9 nm to 554.4 nm (Raman shifts of 377 cm^{-1} to 759 cm^{-1}). This range

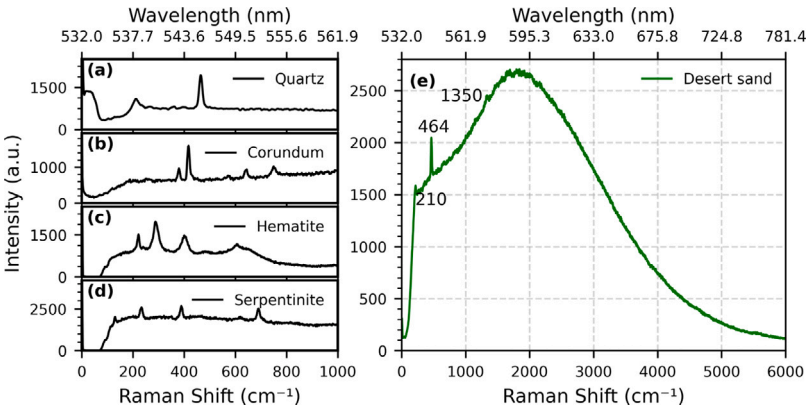

Fig. 10. Raman spectra of various dust components and their spectral signatures below 800 cm^{-1}: (a) quartz, (b) corundum, (c) hematite, (d) serpentinite, and (e) desert sand measured in the LITES laboratory using Raman microscope.

encompasses characteristic vibrational modes of various desert dust components, including quartz (~464 cm^{-1}), corundum (~417 cm^{-1}), feldspars (~510 cm^{-1}), clay minerals such as kaolinite (~635 cm^{-1}), and iron oxides such as hematite (~290 cm^{-1}) (Yadav et al., 2025). We obtained Raman spectra of these minerals using our Raman microscope at the LITES laboratory. For reference, the results are shown in Fig. 10(a–d). The absence of distinct Raman peaks below 800 cm^{-1} can be attributed to the lower spectral resolution of the lidar system's spectroscopic channels. The smoothly decreasing trend observed in the logarithmic spectra between 542.9 and 554.4 nm may also be associated with fluorescence from specific mineral dust components. Reichardt et al. (2025) recently analyzed the fluorescence spectra of Saharan dust transported over Germany and reported a maximum at ~455 nm followed by a gradual decrease extending to ~680 nm. Although their study used a 355 nm excitation wavelength, the observed spectral slope is comparable to that seen in our measurements. At this stage, with the currently available data, we cannot conclusively determine whether the spectra in Fig. 9 are governed solely by Raman scattering, fluorescence, or a combination of both processes.

Fig. 11(a) further compares spectra from a low-level cloud (3–4 km) with the dust layer underneath during 22:00–23:00 UTC. We compared the cloud spectrum to the dust spectra in the altitude intervals of 0.5–1 km, 1–2 km, 2–3 km, and the integrated dust layer (0.5–3 km). This comparison highlights clear altitude-dependent spectral variations within the spectra. Across all dust spectra, a persistent spectral feature near 571.0 ± 1.3 nm (1284 ± 40 cm^{-1}) is observed, which is consistent with the findings shown in Fig. 9. In contrast, this feature is absent in the cloud spectrum (3–4 km), which confirms its association with the dust layer rather than with cloud water droplets. The absence of this spectral signature in the cloud layer further validates the attribution of this peak to the dust plume, as identified in the earlier time-averaged profiles. Furthermore, the higher signal intensity in the shorter wavelength region (542.9–554.4 nm) within the dust layer (Fig. 9) is also evident in Fig. 11(a) across all dust altitude ranges, while it being absent in the cloud spectrum. The absence of such spectral features in the cloud spectrum confirms their attribution to the dust layer and reinforces the capability of spectroscopic lidar measurements to discriminate aerosol types based on their intrinsic vibrational signatures. This feature of spectroscopic lidar allows for effective separation of dust from cloud contributions in atmospheric scenarios where clouds are immersed in aerosol layers. It is worth noting that the high signal intensity observed in the cloud spectrum may be associated with fluorescence emissions or multiple scattering processes within the cloud droplets, which can contribute to the overall spectral characteristics.

To further quantify this distinction, linear fits were applied to the logarithm of the ratios of spectral signals to the oxygen signal for spectra from 0.5–1 km, 1–2 km, 2–3 km, the integrated dust layer (0.5–3 km), and the lower cloud (3–4 km), as shown in Fig. 11(b). The slopes/nm, summarized in Table 2, are consistently around −0.08/nm for all dust layer spectra compared with −0.03/nm for the lower cloud. These differences further confirm that the higher signal intensities in the shorter-wavelength region are attributable to mineral dust. Finally, the reliability of these features is supported by the percentage relative errors of the photon counts (Fig. 12), which show that all spectra below 3–4 km maintain relative errors under 10%. This confirms the robustness of the observed peak and the higher signal intensities in the initial channels.

Table 2
Linear regression slopes and R^2 values for different altitude ranges.

Spectrum	Slope/nm	R^2
0.5–1.0 km	−0.066	0.9547
1.0–2.0 km	−0.079	0.9801
2.0–3.0 km	−0.088	0.9801
0.5–3.0 km (Dust layer)	−0.082	0.9804
3.0–4.0 km (Low cloud)	−0.029	0.8587

4. Discussion

The CAMS reanalysis provides complementary information on dust optical depth. A value of 0.24 at 550 nm during the peak of the event shows excellent consistency with the lidar-derived observations. Furthermore, ground-based AERONET measurements also reveal a good agreement. Daily averaged coarse-mode AOD values of 0.25, 0.37, and 0.27 were recorded at the Lille, Bayfordbury, and University of Manchester stations, respectively, at 500 nm. The lidar-derived dust optical depth values are 0.19–0.26 (2–5 km altitude) at 532 nm. These values are generally lower than previously reported lidar-based measurements across Europe. For example, Gobbi et al. (2000) reported values of 0.1–0.2 prior to and after the dust event, with a maximum of 0.6 at 532 nm during Mediterranean dust events, while Müller et al. (2003) recorded dust optical depths of 0.25–0.63 at 532 nm over central Europe, and Ansmann et al. (2003) reported 0.1–0.5 (reaching 0.8) at 532 nm during long-range transport episodes over northern Europe. Based on the particle-loading classification at 532 nm by López-Cayuela et al. (2025), which defines dust events as low (DAOD < 0.2), moderate (0.2–0.5), or intense (0.5–1.0), indicates that the present case falls within the low-to-moderate category, highlighting a relatively weaker intrusion compared to stronger Saharan dust outbreaks across Europe.

The lidar ratios (53 ± 14 sr and 51 ± 11 sr) and particle linear depolarization ratios (0.27 ± 0.02 and 0.28 ± 0.01) at 532 nm are typical values of Saharan dust observed over Europe (Papayannis et al., 2008; Soupiona et al., 2020; Haarig et al., 2022; Ansmann et al., 2003;

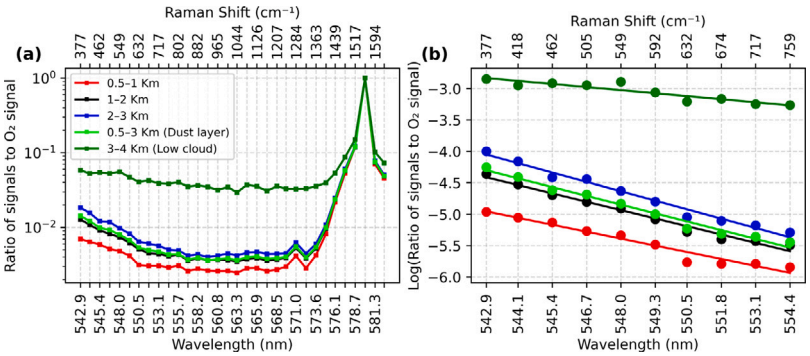

Fig. 11. (a) Comparative spectral profiles of lidar signals between cloud and dust layers observed from 22:00–23:00 UTC. All spectra are normalized to the oxygen Raman channel at 580.0 nm. (b) Linear regression fits of the log-normalized count rate versus wavelength for the same spectra: 0.5–1 km (red), 1–2 km (black), 2–3 km (blue), dust (lime), and low cloud (green). Data points are shown as markers, and the corresponding fits as solid lines, applied to the higher signal intensity region between 542.9 and 554.4 nm.

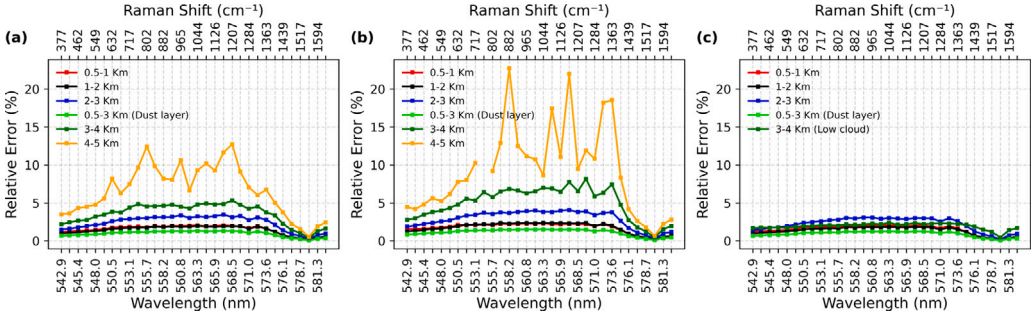

Fig. 12. Percentage relative errors of photon count measurements of spectra measured during (a) 20:30–21:20 UTC, (b) 23:15–23:59 UTC, and (c) 22:00–23:00 UTC.

Mattis et al., 2002; Müller et al., 2003). Transported Saharan dust exhibits considerable variability in the lidar ratio and depolarization ratio due to chemical processing, removal mechanisms, and mixing processes. Near-source measurements from Morocco (SAMUM 2006) and the Cape Verde Islands show reference values for pure Saharan dust: depolarization ratios of 0.27–0.35 (mean: 0.31) and lidar ratios of 56–63 sr at 532 nm (Tesche et al., 2009; Freudenthaler et al., 2009; Groß et al., 2011b,a). European observations document broader ranges reflecting transport effects: southern/central Europe shows lidar ratios of 30–80 sr (mean: 50–60 sr) and depolarization ratios of 0.24–0.28 (EARLINET studies) (Papayannis et al., 2008; Soupiona et al., 2020), while northern Europe exhibits wider variability with depolarization ratios of 0.15–0.25 and lidar ratios of 40–80 sr due to long-range transport and mixing with anthropogenic aerosols (Ansmann et al., 2003; Mattis et al., 2002). The variations in lidar and particle depolarization ratios can be influenced by dust transport pathways and atmospheric interactions. Short-range transported Saharan dust, which directly intrudes into southern Europe, retains its high lidar and depolarization ratios, indicating minimal modification. For instance, Müller et al. (2009) reported similar lidar ratio values over Morocco (northern-Africa) and Southern Europe. Long-range transported dust, typically found over central and northern Europe, exhibits signs of interaction with urban pollution, leading to a decrease in the lidar ratio and the particle linear depolarization ratio due to the presence of anthropogenic aerosols. These transformations highlight the significant impact of transport distance and atmospheric processing on dust optical properties.

Our lidar ratio and particle depolarization values align with Saharan dust, but slightly reduced depolarization was observed in the lower altitude plume. Such reductions likely reflect the influx of fine-mode particles during transport, but may also be influenced by plume dynamics (e.g., layer convergence or dispersion), boundary-layer interactions, or mixing with local aerosols. The lower depolarization values (0.22 ± 0.02 and 0.20 ± 0.01) observed near the plume base, together with an increased fine-mode AOD contribution (24% to 33%) from AERONET stations at Lille and UoM, are consistent with these mechanisms. While our dataset does not allow us to isolate the dominant process, HYSPLIT back trajectories (Fig. 5) suggest that air parcels below 2 km likely mixed with urban pollution during transport. The retrieval of the Ångström exponent from lidar data was limited by the instrument configuration, preventing us from conducting a more robust size-distribution analysis.

A key advancement of this study is the identification of lidar-derived spectra using a spectroscopic lidar. The persistence of the 571.0 ± 1.3 nm (1284 ± 40 cm^{-1}) spectral feature up to 3–4 km altitude, which is absent in the cloud spectrum, highlights its significance as a robust dust signature, providing strong evidence that spectroscopic lidar can capture mineral-specific vibrational modes under ambient conditions. Higher intensity signals in the 542.9–554.4 nm range, corresponding to vibrational modes of various dust components, including silicates, clays, feldspars, and iron oxides (Yadav et al., 2025), further emphasize the technique's sensitivity to compositional diversity. Together with spectral slope analysis, these results show that spectroscopic lidar can be a powerful tool for aerosol typing based on the use of spectral signatures. Despite the intrinsically weak Raman signals from dust, the reliable detection of these features underscores the feasibility of this approach, even under relatively low dust loadings. These findings highlight the complementary roles of conventional

optical parameters (sensitive to size, shape, and mixing state) and Raman spectral signatures (directly tied to dust's chemical composition). Together, they allow for a more robust discrimination of dust layers in complex atmospheric conditions, particularly in cases of dust–cloud mixed atmospheric scenarios.

Earlier efforts exploring the capabilities of Raman lidar for the mineralogical analysis of Asian dust focused primarily on quartz. Tatarov and Sugimoto (2005) first demonstrated quartz retrievals using the 464 cm^{-1} (361 nm with 355 nm excitation) vibrational mode. Later, Müller et al. (2010) confirmed that such signals could be extracted even in mixed dust–haze conditions. Our results extend these efforts by moving from single-mineral detection to broader mineral fingerprinting through the identification of multiple vibrational modes. This advance highlights the potential of spectroscopic lidar to provide a more comprehensive characterization of dust composition. The unidentified feature at 1284 ± 40 cm^{-1}, however, illustrates a current limitation: without laboratory-determined Raman scattering cross-sections for key minerals, quantitative retrievals remain uncertain. Targeted laboratory studies will therefore be essential for translating spectroscopic lidar into a tool for robust, component-specific dust analysis.

Despite these advancements, several constraints must be acknowledged. Raman backscatter signals are inherently weak, and their retrieval is highly sensitive to detector efficiency, photon-counting statistics, and intense background solar radiation. Low dust concentration may also limit the signal-to-noise ratio, causing the spectral signatures indistinct. Coarser spectral resolution of the lidar spectrometer (1.3 nm, ~40 cm^{-1}) limits direct comparison with laboratory Raman spectra (0.05 nm, 1–2 cm^{-1}). Furthermore, limited spectral coverage (only 40 nm with a 600 grooves/mm grating) restricts the longer Raman shift region. For example, our interest in the lower Raman shift region in this case, prevented us from including the nitrogen channel, but in turn allowed us to use oxygen Raman signals.

Oxygen is comparably little explored in Raman lidar technology. The limited spectral coverage thus offered the chance to test, for example, the advantages of using oxygen signals for calibrating lidar signals. Another advantage of using oxygen for lidar-signal calibration lies in the fact that silicates and other major dust minerals (aluminosilicates, oxides, clays, feldspars, hematite, etc.) contain oxygen as a key structural element (Si–O, Si–O–Si, Fe–O, Al–O, etc.). Therefore, we can make use of the oxygen Raman signal not only as a stable atmospheric reference for calibration, but also as a spectrally relevant baseline when interpreting vibrational modes of oxygen-bearing dust components. Dust vibrational bands (oxygen-containing minerals) are closer to the oxygen Raman line (~1555 cm^{-1}) compared to the nitrogen Raman line (~2330 cm^{-1}) (Weitkamp, 2005), which reduces the systematic uncertainties associated with comparing widely separated Raman channels. The use of oxygen Raman signals furthermore enhances the discriminatory capability of Raman lidar for identifying dust-specific oxygen vibrational features.

Looking forward, exploiting oxygen Raman signals could open the door to more advanced mineralogical retrievals, where the well-characterized atmospheric oxygen serves as a reference against which weak but composition-specific dust bands can be normalized. If a consistent scaling relationship can be established (e.g., using lab spectra of mineral mixtures), the oxygen Raman line could help in semi-quantitative retrievals of dust mineral components since mineral-specific Raman scattering cross-sections are not well established. This approach could ultimately strengthen the use of spectroscopic lidar for quantitative dust mineralogy, bridging the gap between atmospheric calibration and chemical/mineral fingerprinting. Future improvements in spectral resolution, sensitivity, and wavelength coverage will be essential for advancing the use of spectroscopic lidar in dust characterization capabilities.

5. Conclusion

This study presents the first 532 nm lidar-based characterization of Saharan dust transport over the UK, complemented by spectroscopic observations of dust Raman signatures. Dust optical depths of 0.19–0.26 at 532 nm were observed within the 2–5 km altitude range. The lidar ratios were approximately 51–53 sr, and the particle linear depolarization ratios were approximately 0.27–0.28 at 532 nm in the center of the dust plume. We find good consistency with CAMS reanalysis data, which showed a dust optical depth of 0.24 at 550 nm. Our results are supported by AERONET observations that were carried out southeast of our lidar site (Lille), near it (Bayfordbury), and northwest of it (Manchester). High aerosol optical depths (0.4–0.7 at 500 nm) and low Ångström exponents (0.05–0.2) are indicative of dust-dominated conditions. Coarse-mode AOD values were 0.25–0.37 at 500 nm. Additionally, the AERONET observations revealed a gradual increase in the fine-mode contribution to total AOD along the transport path from Lille (24%) in France to Bayfordbury (26%) and Manchester (33%) in the UK. Our lidar observations also showed reduced depolarization values of approximately 0.2 in the lower altitude of the dust plume, which suggests particle modification processes that could result from either local boundary layer interactions or mixing during long-range transport.

The observed optical parameters align well with previously documented European observations of transported Saharan dust. Southern and central European measurements typically show lidar ratios (mean) of 50–60 sr and depolarization ratios of 0.24–0.28, while northern European sites exhibit broader variability due to long-range transport effects and anthropogenic aerosol mixing. The challenge of discriminating dust properties in the presence of local aerosols, particularly at lower altitudes where HYSPLIT trajectories suggest interaction with pollution sources, adds more complexity to accurately distinguishing the aerosol types using traditional optical-based retrievals. This complexity increases further when clouds are embedded within dust layers, which makes conventional aerosol typing approaches a highly challenging task and highlights the need for complementary identification methods. One of such novel methods is Raman-spectroscopy by lidar, which allows for an improved aerosol-type discrimination based on the intrinsic rotational-vibrational signatures of the chemical components in particles. We present, to the best of our knowledge, the first observations of a Saharan dust event using a Raman spectroscopic lidar developed at the University of Hertfordshire. In the present case, even under moderate loading, the detection of a persistent Raman peak at 571.0 ± 1.3 nm (1284 ± 40 cm^{-1}) and higher signals in the 542.9–554.4 nm shows that spectroscopic lidar can identify mineral-specific vibrational signatures, even under relatively weak dust conditions. We furthermore find that the absence of such spectral features in the cloud spectrum and outside the dust plume confirms the direct association of these features with dust particles and demonstrates the discriminatory capability of the spectroscopic technique in the complex atmospheric environment. We also identified that the higher signal intensity in the 542.9–554.4 nm range, aligns well with the spectral region of the vibrational modes of the prominent dust component (i.e., silicates, clays, feldspars, and iron oxides) based on laboratory measurements of dust samples, we carried out with our Raman-microscope.

A key lesson of our study is that even when discrete mineral signatures are not detectable under moderate dust loadings, robust spectral patterns can still be retrieved. This underscores both the promise of using spectrally resolved lidar observations and the limitations imposed by weak Raman signals, low spectral resolution, and low dust concentration. Future developments should prioritize improving instrument sensitivity and spectral resolution to enable distinct component-specific spectral signatures and quantitative concentration retrievals. Integration with advanced modeling and laboratory experiments of differential

Raman scattering cross-sections could transform spectroscopic lidar from a qualitative identification tool into a quantitative compositional analysis platform, significantly enhancing our ability to monitor and understand atmospheric mineral dust on a routine basis.

CRediT authorship contribution statement

Avinash C. Yadav: Writing – review & editing, Writing – original draft, Visualization, Validation, Software, Methodology, Investigation, Formal analysis, Data curation. **Boyan Tatarov:** Writing – review & editing, Supervision, Resources, Conceptualization. **Rui Song:** Writing – review & editing, Software, Formal analysis, Data curation. **Adrian Ghita:** Writing – review & editing. **Detlef Müller:** Writing – review & editing, Supervision, Resources, Conceptualization.

Funding

This research was supported by the University of Hertfordshire, United Kingdom through capital investment, a part of which was provided by QR funding. QR refers to Quality-Related funding, a form of government support provided to UK universities based on the quality of their research, assessed through the national Research Excellence Framework (REF). Boyan Tatarov was supported by a Marie-Skłodowska-Curie Action Fellowship of the European Commission (CAPABLE, H2020-MSCA-IF-2015), Grant No: 708227. Detlef Müller was supported by the Royal Society, United Kingdom (WM120052).

Declaration of competing interest

The authors declare that they have no known competing financial interests or personal relationships that could have appeared to influence the work reported in this paper.

Acknowledgments

The authors acknowledge the Copernicus Atmosphere Monitoring Service (CAMS), which provided air quality forecasts and the reanalysis datasets of dust concentration and optical depth at European and global scales. We acknowledge the use of imagery from the NASA Worldview application (https://worldview.earthdata.nasa.gov), part of the NASA Earth Observing System Data and Information System (EOSDIS).

The authors gratefully acknowledge the NOAA Air Resources Laboratory (ARL) for the provision of the HYSPLIT transport and dispersion model and/or READY website (https://www.ready.noaa.gov) used in this publication.

We thank the Principal Investigators and their staff for establishing and maintaining the AERONET sites at Lille, Bayfordbury, and UoM used in this work.

The authors gratefully acknowledge Prof. Konrad Kandler, University of Darmstadt, for preparing and providing the dust samples for the laboratory investigation.

We also thank the anonymous reviewers for their valuable comments and suggestions.

Data availability

Data will be made available on request.

References

Ansmann, A., Bösenberg, J., Chaikovsky, A., Comerón, A., Eckhardt, S., Eixmann, R., Freudenthaler, V., Ginoux, P., Komguem, L., Linné, H., Márquez, M.Á.L., Matthias, V., Mattis, I., Mitev, V., Müller, D., Music, S., Nickovic, S., Pelon, J., Sauvage, L., Sobolewsky, P., Srivastava, M.K., Stohl, A., Torres, O., Vaughan, G., Wandinger, U., Wiegner, M., 2003. Long-range transport of Saharan dust to northern Europe: The 11–16 October 2001 outbreak observed with EARLINET. J. Geophys. Res. Atmospheres 108 (D24), 4783. http://dx.doi.org/10.1029/2003jd003757.

Ansmann, A., Müller, D., 2005. Lidar and atmospheric aerosol particles. In: Lidar: Range-Resolved Optical Remote Sensing of the Atmosphere. Springer New York, New York, NY, pp. 105–141. http://dx.doi.org/10.1007/0-387-25101-4_4, Chapter 4.

Ansmann, A., Riebesell, M., Weitkamp, C., 1990. Measurement of atmospheric aerosol extinction profiles with a Raman lidar. Opt. Lett. 15 (13), 746. http://dx.doi.org/10.1364/ol.15.000746.

Ansmann, A., Wandinger, U., Riebesell, M., Weitkamp, C., Michaelis, W., 1992. Independent measurement of extinction and backscatter profiles in cirrus clouds by using a combined Raman elastic-backscatter lidar. Appl. Opt. 31 (33), 7113. http://dx.doi.org/10.1364/ao.31.007113.

Atkinson, J.D., Murray, B.J., Woodhouse, M.T., Whale, T.F., Baustian, K.J., Carslaw, K.S., Dobbie, S., O'Sullivan, D., Malkin, T.L., 2013. The importance of feldspar for ice nucleation by mineral dust in mixed-phase clouds. Nature 498 (7454), 355–358. http://dx.doi.org/10.1038/nature12278.

Balis, D., Amiridis, V., Kazadzis, S., Papayannis, A., Tsaknakis, G., Tzortzakis, S., Kalivitis, N., Vrekoussis, M., Kanakidou, M., Mihalopoulos, N., Chourdakis, G., Nickovic, S., Pérez, C., Baldasano, J., Drakakis, M., 2006. Optical characteristics of desert dust over the East Mediterranean during summer: A case study. Ann. Geophys. 24 (3), 807–821. http://dx.doi.org/10.5194/angeo-24-807-2006.

Behrendt, A., Nakamura, T., 2002. Calculation of the calibration constant of polarization lidar and its dependency on atmospheric temperature. Opt. Express 10 (16), 805–817. http://dx.doi.org/10.1364/OE.10.000805.

Belegante, L., Bravo-Aranda, J.A., Freudenthaler, V., Nicolae, D., Nemuc, A., Ene, D., Alados-Arboledas, L., Amodeo, A., Pappalardo, G., D'Amico, G., Amato, F., Engelmann, R., Baars, H., Wandinger, U., Papayannis, A., Kokkalis, P., Pereira, S.N., 2018. Experimental techniques for the calibration of lidar depolarization channels in EARLINET. Atmospheric Meas. Tech. 11 (2), 1119–1141. http://dx.doi.org/10.5194/amt-11-1119-2018.

Berger, M., Moreno, J., Johannessen, J.A., Levelt, P.F., Hanssen, R.F., 2012. ESA's sentinel missions in support of Earth system science. Remote Sens. Environ. 120, 84–90. http://dx.doi.org/10.1016/j.rse.2011.07.023.

Bi, H., Chen, S., Zhang, D., Wang, Y., Kang, L., Alam, K., Tang, M., Chen, Y., Zhang, Y., Wang, D., 2024. The circumglobal transport of massive African dust and its impacts on the regional circulation in remote atmosphere. Bull. Am. Meteorol. Soc. 105 (3), E605–E622. http://dx.doi.org/10.1175/bams-d-23-0072.1.

Biele, J., Beyerle, G., Baumgarten, G., 2000. Polarization lidar: Correction of instrumental effects. Opt. Express 7, 427–435.

Bravo-Aranda, J.A., Belegante, L., Freudenthaler, V., Alados-Arboledas, L., Nicolae, D., Granados-Muñoz, M.J., Guerrero-Rascado, J.L., Amodeo, A., D'Amico, G., Engelmann, R., Pappalardo, G., Kokkalis, P., Mamouri, R., Papayannis, A., Navas-Guzmán, F., Olmo, F.J., Wandinger, U., Amato, F., Haeffelin, M., 2016. Assessment of lidar depolarization uncertainty by means of a polarimetric lidar simulator. Atmospheric Meas. Tech. 9 (10), 4935–4953. http://dx.doi.org/10.5194/amt-9-4935-2016.

Cao, C., De Luccia, F.J., Xiong, X., Wolfe, R., Weng, F., 2014. Early on-orbit performance of the visible infrared imaging radiometer suite onboard the Suomi National Polar-Orbiting Partnership (S-NPP) satellite. IEEE Trans. Geosci. Remote Sens. 52 (2), 1142–1156. http://dx.doi.org/10.1109/tgrs.2013.2247768.

Cao, C., Xiong, J., Blonski, S., Liu, Q., Uprety, S., Shao, X., Bai, Y., Weng, F., 2013. Suomi NPP VIIRS sensor data record verification, validation, and long-term performance monitoring. J. Geophys. Res. Atmospheres 118 (20), 11664–11678. http://dx.doi.org/10.1002/2013jd020418.

Dubovik, O., King, M.D., 2000. A flexible inversion algorithm for retrieval of aerosol optical properties from sun and sky radiance measurements. J. Geophys. Res. Atmospheres 105 (D16), 20673–20696. http://dx.doi.org/10.1029/2000jd900282.

Dubovik, O., Smirnov, A., Holben, B.N., King, M.D., Kaufman, Y.J., Eck, T.F., Slutsker, I., 2000. Accuracy assessments of aerosol optical properties retrieved from Aerosol Robotic Network (AERONET) sun and sky radiance measurements. J. Geophys. Res. Atmospheres 105 (D8), 9791–9806. http://dx.doi.org/10.1029/2000jd900040.

Dunion, J.P., Velden, C.S., 2004. The impact of the Saharan air layer on Atlantic tropical cyclone activity. Bull. Am. Meteorol. Soc. 85 (3), 353–366. http://dx.doi.org/10.1175/bams-85-3-353.

Eck, T.F., Holben, B.N., Reid, J.S., Arola, A., Ferrare, R.A., Hostetler, C.A., Crumeyrolle, S.N., Berkoff, T.A., Welton, E.J., Lolli, S., Lyapustin, A., Wang, Y., Schafer, J.S., Giles, D.M., Anderson, B.E., Thornhill, K.L., Minnis, P., Pickering, K.E., Loughner, C.P., Smirnov, A., Sinyuk, A., 2014. Observations of rapid aerosol optical depth enhancements in the vicinity of polluted cumulus clouds. Atmospheric Chem. Phys. 14 (21), 11633–11656. http://dx.doi.org/10.5194/acp-14-11633-2014.

Esselborn, M., Wirth, M., Fix, A., Weinzierl, B., Rasp, K., Tesche, M., Petzold, A., 2009. Spatial distribution and optical properties of Saharan dust observed by airborne high spectral resolution lidar during SAMUM 2006. Tellus B: Chem. Phys. Meteorol. 61 (1), 131. http://dx.doi.org/10.1111/j.1600-0889.2008.00394.x.

Fernald, F.G., 1984. Analysis of atmospheric lidar observations: Some comments. Appl. Opt. 23 (5), 652–653. http://dx.doi.org/10.1364/AO.23.000652.

Floutsi, A.A., Baars, H., Engelmann, R., Althausen, D., Ansmann, A., Bohlmann, S., Heese, B., Hofer, J., Kanitz, T., Haarig, M., Ohneiser, K., Radenz, M., Seifert, P., Skupin, A., Yin, Z., Abdullaev, S.F., Komppula, M., Filioglou, M., Giannakaki, E., Stachlewska, I.S., Janicka, L., Bortoli, D., Marinou, E., Amiridis, V., Gialitaki, A.,

Mamouri, R.-E., Barja, B., Wandinger, U., 2023. DeLiAn – a growing collection of depolarization ratio, lidar ratio and Ångström exponent for different aerosol types and mixtures from ground-based lidar observations. Atmospheric Meas. Tech. 16 (9), 2353–2379. http://dx.doi.org/10.5194/amt-16-2353-2023.

Freudenthaler, V., 2016. About the effects of polarising optics on lidar signals and the Δ90 calibration. Atmospheric Meas. Tech. 9 (9), 4181–4255. http://dx.doi.org/10.5194/amt-9-4181-2016.

Freudenthaler, V., Esselborn, M., Wiegner, M., Heese, B., Tesche, M., Ansmann, A., Müller, D., Althausen, D., Wirth, M., Fix, A., Ehret, G., Knippertz, P., Toledano, C., Gasteiger, J., Garhammer, M., Seefeldner, M., 2009. Depolarization ratio profiling at several wavelengths in pure Saharan dust during SAMUM 2006. Tellus B 61 (1), 165–179. http://dx.doi.org/10.1111/j.1600-0889.2008.00396.x.

Giles, D.M., Sinyuk, A., Sorokin, M.G., Schafer, J.S., Smirnov, A., Slutsker, I., Eck, T.F., Holben, B.N., Lewis, J.R., Campbell, J.R., Welton, E.J., Korkin, S.V., Lyapustin, A.I., 2019. Advancements in the Aerosol Robotic Network (AERONET) version 3 database – automated near-real-time quality control algorithm with improved cloud screening for sun photometer aerosol optical depth (AOD) measurements. Atmospheric Meas. Tech. 12 (1), 169–209. http://dx.doi.org/10.5194/amt-12-169-2019.

Gobbi, G.P., Barnaba, F., Giorgi, R., Santacasa, A., 2000. Altitude-resolved properties of a Saharan dust event over the Mediterranean. Atmos. Environ. 34 (29), 5119–5127. http://dx.doi.org/10.1016/S1352-2310(00)00194-1, Sixth Scientific Conference of the International Global Atmospheric.

Groß, S., Tesche, M., Freudenthaler, V., Toledano, C., Wiegner, M., Ansmann, A., Althausen, D., and, M.S., 2011a. Characterization of Saharan dust, marine aerosols and mixtures of biomass-burning aerosols and dust by means of multi-wavelength depolarization and Raman lidar measurements during SAMUM 2. Tellus B: Chem. Phys. Meteorol. 63 (4), 706–724. http://dx.doi.org/10.1111/j.1600-0889.2011.00556.x.

Groß, S., Wiegner, M., Freudenthaler, V., Toledano, C., 2011b. Lidar ratio of Saharan dust over Cape Verde islands: Assessment and error calculation. J. Geophys. Res. Atmospheres 116 (D15), D15203. http://dx.doi.org/10.1029/2010JD015435.

Gutleben, M., Groß, S., Heske, C., Wirth, M., 2022. Wintertime Saharan dust transport towards the Caribbean: An airborne lidar case study during EUREC^{4}A. Atmospheric Chem. Phys. 22 (11), 7319–7330. http://dx.doi.org/10.5194/acp-22-7319-2022.

Haarig, M., Ansmann, A., Engelmann, R., Baars, H., Toledano, C., Torres, B., Althausen, D., Radenz, M., Wandinger, U., 2022. First triple-wavelength lidar observations of depolarization and extinction-to-backscatter ratios of Saharan dust. Atmospheric Chem. Phys. 22 (1), 355–369. http://dx.doi.org/10.5194/acp-22-355-2022.

Hsu, N.C., Jeong, M.-J., Bettenhausen, C., Sayer, A.M., Hansell, R., Seftor, C.S., Huang, J., Tsay, S.-C., 2013. Enhanced Deep Blue aerosol retrieval algorithm: The second generation. J. Geophys. Res. Atmospheres 118 (16), 9296–9315. http://dx.doi.org/10.1002/jgrd.50712.

Hsu, N.C., Lee, J., Sayer, A.M., Kim, W., Bettenhausen, C., Tsay, S.-C., 2019. VIIRS Deep Blue aerosol products over land: Extending the EOS long-term aerosol data records. J. Geophys. Res. Atmospheres 124 (7), 4026–4053. http://dx.doi.org/10.1029/2018jd029688.

Jackson, J.M., Liu, H., Laszlo, I., Kondragunta, S., Remer, L.A., Huang, J., Huang, H.-C., 2013. Suomi-NPP VIIRS aerosol algorithms and data products. J. Geophys. Res. Atmospheres 118 (22), 12673–12689. http://dx.doi.org/10.1002/2013jd020449.

Kahn, R.A., Liu, Y., Diner, D.J., 2023. Space-based passive aerosol remote sensing from the multi-angle imaging SpectroRadiometer (MISR) aboard NASA's Terra satellite. In: Handbook of Air Quality and Climate Change. Springer Nature Singapore, Singapore, pp. 307–320. http://dx.doi.org/10.1007/978-981-15-2760-9_62.

Kaufman, Y.J., Koren, I., Remer, L.A., Tanré, D., Ginoux, P., Fan, S., 2005. Dust transport and deposition observed from the Terra-Moderate Resolution Imaging Spectroradiometer (MODIS) spacecraft over the Atlantic ocean. J. Geophys. Res. Atmospheres 110 (D10), S12. http://dx.doi.org/10.1029/2003jd004436.

Kinne, S., Schulz, M., Textor, C., Guibert, S., Balkanski, Y., Bauer, S.E., Berntsen, T., Berglen, T.F., Boucher, O., Chin, M., Collins, W., Dentener, F., Diehl, T., Easter, R., Feichter, J., Fillmore, D., Ghan, S., Ginoux, P., Gong, S., Grini, A., Hendricks, J., Herzog, M., Horowitz, L., Isaksen, I., Iversen, T., Kirkevåg, A., Kloster, S., Koch, D., Kristjansson, J.E., Krol, M., Lauer, A., Lamarque, J.F., Lesins, G., Liu, X., Lohmann, U., Montanaro, V., Myhre, G., Penner, J., Pitari, G., Reddy, S., Seland, O., Stier, P., Takemura, T., Tie, X., 2006. An AeroCom initial assessment – optical properties in aerosol component modules of global models. Atmospheric Chem. Phys. 6 (7), 1815–1834. http://dx.doi.org/10.5194/acp-6-1815-2006.

Klett, J.D., 1981. Stable analytical inversion solution for processing lidar returns. Appl. Opt. 20 (2), 211. http://dx.doi.org/10.1364/ao.20.000211.

Kong, S., Sato, K., Bi, L., 2022. Lidar ratio–depolarization ratio relations of atmospheric dust aerosols: The super-spheroid model and high spectral resolution lidar observations. J. Geophys. Res. Atmospheres 127 (4), e2021JD035629. http://dx.doi.org/10.1029/2021JD035629.

Liu, Z., Omar, A., Vaughan, M., Hair, J., Kittaka, C., Hu, Y., Powell, K., Trepte, C., Winker, D., Hostetler, C., Ferrare, R., Pierce, R., 2008. CALIPSO lidar observations of the optical properties of Saharan dust: A case study of long-range transport. J. Geophys. Res. Atmospheres 113 (D7), 07207. http://dx.doi.org/10.1029/2007jd008878.

López-Cayuela, M.-Á., Córdoba-Jabonero, C., Sicard, M., Abril-Gago, J., Salgueiro, V., Comerón, A., Granados-Muñoz, M.J., Costa, M.J., Muñoz-Porcar, C., Bravo-Aranda, J.A., Bortoli, D., Rodríguez-Gómez, A., Alados-Arboledas, L., Guerrero-Rascado, J.L., 2025. Fine and coarse dust radiative impact during an intense Saharan dust outbreak over the Iberian Peninsula – short-wave direct radiative effect. Atmospheric Chem. Phys. 25 (5), 3213–3231. http://dx.doi.org/10.5194/acp-25-3213-2025.

Mahowald, N.M., Baker, A.R., Bergametti, G., Brooks, N., Duce, R.A., Jickells, T.D., Kubilay, N., Prospero, J.M., Tegen, I., 2005. Atmospheric global dust cycle and iron inputs to the ocean. Glob. Biogeochem. Cycles 19 (4), GB4025. http://dx.doi.org/10.1029/2004gb002402.

Mahowald, N.M., Engelstaedter, S., Luo, C., Sealy, A., Artaxo, P., Benitez-Nelson, C., Bonnet, S., Chen, Y., Chuang, P.Y., Cohen, D.D., Dulac, F., Herut, B., Johansen, A.M., Kubilay, N., Losno, R., Maenhaut, W., Paytan, A., Prospero, J.M., Shank, L.M., Siefert, R.L., 2009. Atmospheric iron deposition: Global distribution, variability, and human perturbations. Annu. Rev. Mar. Sci. 1 (1), 245–278. http://dx.doi.org/10.1146/annurev.marine.010908.163727.

Malenovský, Z., Rott, H., Cihlar, J., Schaepman, M.E., García-Santos, G., Fernandes, R., Berger, M., 2012. Sentinels for science: Potential of sentinel-1, -2, and -3 missions for scientific observations of ocean, cryosphere, and land. Remote Sens. Environ. 120, 91–101. http://dx.doi.org/10.1016/j.rse.2011.09.026.

Mattis, I., Ansmann, A., Müller, D., Wandinger, U., Althausen, D., 2002. Dual-wavelength Raman lidar observations of the extinction-to-backscatter ratio of Saharan dust. Geophys. Res. Lett. 29 (9), 29. http://dx.doi.org/10.1029/2002gl014721.

Molesworth, A.M., Cuevas, L.E., Connor, S.J., Morse, A.P., Thomson, M.C., 2003. Environmental risk and meningitis epidemics in Africa. Emerg. Infect. Dis. 9 (10), 1287–1293. http://dx.doi.org/10.3201/eid0910.030182.

Müller, D., Heinold, B., Tesche, M., Tegen, I., Althausen, D., Arboledas, L.A., Amiridis, V., Amodeo, A., Ansmann, A., Balis, D., Comeron, A., D'amico, G., Gerasopoulos, E., Guerrero-Rascado, J.L., Freudenthaler, V., Giannakaki, E., Heese, B., Iarlori, M., Knippertz, P., Mamouri, R.E., Mona, L., Papayannis, A., Pappalardo, G., Perrone, R.M., Pisani, G., Rizi, V., Sicard, M., Spinelli, N., Tafuro, A., Wiegner, M., 2009. EARLINET observations of the 14–22-May long-range dust transport event during SAMUM 2006: Validation of results from dust transport modelling. Tellus B: Chem. Phys. Meteorol. 61 (1), 325. http://dx.doi.org/10.1111/j.1600-0889.2008.00400.x.

Müller, D., Mattis, I., Tatarov, B., Noh, Y.M., Shin, D.H., Shin, S.K., Lee, K.H., Kim, Y.J., Sugimoto, N., 2010. Mineral quartz concentration measurements of mixed mineral dust/urban haze pollution plumes over Korea with multiwavelength aerosol Raman-quartz lidar. Geophys. Res. Lett. 37 (20), L20810. http://dx.doi.org/10.1029/2010GL044633.

Müller, D., Mattis, I., Wandinger, U., Ansmann, A., Althausen, D., Dubovik, O., Eckhardt, S., Stohl, A., 2003. Saharan dust over a central European EARLINET-AERONET site: Combined observations with Raman lidar and sun photometer. J. Geophys. Res. Atmospheres 108 (D12), 4345. http://dx.doi.org/10.1029/2002jd002918.

Murayama, T., Sugimoto, N., Uno, I., Kinoshita, K., Aoki, K., Hagiwara, N., Liu, Z., Matsui, I., Sakai, T., Shibata, T., Arao, K., Sohn, B.-J., Won, J.-G., Yoon, S.-C., Li, T., Zhou, J., Hu, H., Abo, M., Iokibe, K., Koga, R., Iwasaka, Y., 2001. Ground-based network observation of Asian dust events of April 1998 in east Asia. J. Geophys. Res. Atmospheres 106 (D16), 18345–18359. http://dx.doi.org/10.1029/2000jd900554.

Osborne, M., Malavelle, F.F., Adam, M., Buxmann, J., Sugier, J., Marenco, F., Haywood, J., 2019. Saharan dust and biomass burning aerosols during ex-hurricane ophelia: Observations from the new UK lidar and sun-photometer network. Atmospheric Chem. Phys. 19 (6), 3557–3578. http://dx.doi.org/10.5194/acp-19-3557-2019.

Papanikolaou, C.-A., Papayannis, A., Gidarakou, M., Abdullaev, S.F., Ajtai, N., Baars, H., Balis, D., Bortoli, D., Bravo-Aranda, J.A., Collaud-Coen, M., de Rosa, B., Dionisi, D., Eleftheratos, K., Engelmann, R., Floutsi, A.A., Abril-Gago, J., Goloub, P., Giuliano, G., Gumà-Claramunt, P., Hofer, J., Hu, Q., Komppula, M., Marinou, E., Martucci, G., Mattis, I., Michailidis, K., Muñoz-Porcar, C., Mylonaki, M., Mytilinaios, M., Nicolae, D., Rodríguez-Gómez, A., Salgueiro, V., Shang, X., Stachlewska, I.S., Ştefănie, H.I., Szczepanik, D.M., Trickl, T., Vogelmann, H., Voudouri, K.A., 2024. Large-scale network-based observations of a Saharan dust event across the European continent in spring 2022. Remote. Sens. 16 (17), 3350. http://dx.doi.org/10.3390/rs16173350.

Papayannis, A., Amiridis, V., Mona, L., Tsaknakis, G., Balis, D., Bösenberg, J., Chaikovski, A., De Tomasi, F., Grigorov, I., Mattis, I., Mitev, V., Müller, D., Nickovic, S., Pérez, C., Pietruczuk, A., Pisani, G., Ravetta, F., Rizi, V., Sicard, M., Trickl, T., Wiegner, M., Gerding, M., Mamouri, R.E., D'Amico, G., Pappalardo, G., 2008. Systematic lidar observations of Saharan dust over Europe in the frame of EARLINET (2000–2002). J. Geophys. Res. Atmospheres 113 (D10), D10204. http://dx.doi.org/10.1029/2007jd009028.

Pappalardo, G., 2007. European aerosol research lidar network-advanced sustainable observation system (EARLINET-ASOS). In: 14th International School on Quantum Electronics: Laser Physics and Applications. Vol. 6604, International Society for Optics and Photonics, SPIE, 66041Y. http://dx.doi.org/10.1117/12.727105.

Pappalardo, G., Amodeo, A., Apituley, A., Comeron, A., Freudenthaler, V., Linné, H., Ansmann, A., Bösenberg, J., D'Amico, G., Mattis, I., Mona, L., Wandinger, U., Amiridis, V., Alados-Arboledas, L., Nicolae, D., Wiegner, M., 2014. EARLINET: Towards an advanced sustainable European aerosol lidar network. Atmospheric Meas. Tech. 7 (8), 2389–2409. http://dx.doi.org/10.5194/amt-7-2389-2014.

Pérez, C., Nickovic, S., Baldasano, J.M., Sicard, M., Rocadenbosch, F., Cachorro, V.E., 2006. A long Saharan dust event over the western Mediterranean: Lidar, sun photometer observations, and regional dust modeling. J. Geophys. Res. Atmospheres 111 (D15), D15214. http://dx.doi.org/10.1029/2005jd006579.

Prenni, A.J., Petters, M.D., Kreidenweis, S.M., Heald, C.L., Martin, S.T., Artaxo, P., Garland, R.M., Wollny, A.G., Pöschl, U., 2009. Relative roles of biogenic emissions and Saharan dust as ice nuclei in the Amazon basin. Nat. Geosci. 2 (6), 402–405. http://dx.doi.org/10.1038/ngeo517.

Prospero, J.M., Collard, F.-X., Molinié, J., Jeannot, A., 2014. Characterizing the annual cycle of African dust transport to the Caribbean basin and South America and its impact on the environment and air quality. Glob. Biogeochem. Cycles 28 (7), 757–773. http://dx.doi.org/10.1002/2013gb004802.

Prospero, J.M., Ginoux, P., Torres, O., Nicholson, S.E., Gill, T.E., 2002. Environmental characterization of global sources of atmospheric soil dust identified with the NIMBUS 7 Total Ozone Mapping Spectrometer (TOMS) absorbing aerosol product. Rev. Geophys. 40 (1), 2–1–2–31. http://dx.doi.org/10.1029/2000RG000095.

Reichardt, J., Lauermann, F., Behrendt, O., 2025. Fluorescence spectra of atmospheric aerosols. Atmospheric Chem. Phys. 25 (11), 5857–5892. http://dx.doi.org/10.5194/acp-25-5857-2025.

Rolph, G., Stein, A., Stunder, B., 2017. Real-time Environmental Applications and Display sYstem: READY. Environ. Model. Softw. 95, 210–228. http://dx.doi.org/10.1016/j.envsoft.2017.06.025.

Sayer, A.M., Hsu, N.C., Lee, J., Bettenhausen, C., Kim, W.V., Smirnov, A., 2018. Satellite Ocean Aerosol Retrieval (SOAR) algorithm extension to S-NPP VIIRS as part of the "Deep Blue" aerosol project. J. Geophys. Res. Atmospheres 123 (1), 380–400. http://dx.doi.org/10.1002/2017jd027412.

Schepanski, K., 2018. Transport of mineral dust and its impact on climate. Geosciences 8 (5), 151. http://dx.doi.org/10.3390/geosciences8050151.

Soupiona, O., Papayannis, A., Kokkalis, P., Foskinis, R., Sánchez Hernández, G., Ortiz-Amezcua, P., Mylonaki, M., Papanikolaou, C.-A., Papagiannopoulos, N., Samaras, S., Groß, S., Mamouri, R.-E., Alados-Arboledas, L., Amodeo, A., Psiloglou, B., 2020. EARLINET observations of Saharan dust intrusions over the northern Mediterranean region (2014–2017):Properties and impact on radiative forcing. Atmospheric Chem. Phys. 20 (23), 15147–15166. http://dx.doi.org/10.5194/acp-20-15147-2020.

Stein, A.F., Draxler, R.R., Rolph, G.D., Stunder, B.J.B., Cohen, M.D., Ngan, F., 2015. NOAA's HYSPLIT atmospheric transport and dispersion modeling system. Bull. Am. Meteorol. Soc. 96 (12), 2059–2077. http://dx.doi.org/10.1175/bams-d-14-00110.1.

Sugimoto, N., Huang, Z., Nishizawa, T., Matsui, I., Tatarov, B., 2012. Fluorescence from atmospheric aerosols observed with a multi-channel lidar spectrometer. Opt. Express 20 (19), 20800–20807. http://dx.doi.org/10.1364/OE.20.020800.

Szczepanik, D.M., Poczta, P., Talianu, C., Böckmann, C., Ritter, C., Stefanie, H., Toanca, F., Chojnicki, B.H., Schüttemeyer, D., Stachlewska, I.S., 2023. Spatio-temporal evolution of long-range transported mineral desert dust properties over rural and urban sites in central Europe. Sci. Total Environ. 903, 166173. http://dx.doi.org/10.1016/j.scitotenv.2023.166173.

Tatarov, B., Müller, D., 2021. LITES: Rotational Raman spectra of air molecules measured by high-resolution-spectroscopy lidar. Opt. Lett. 46 (20), 5173. http://dx.doi.org/10.1364/ol.420070.

Tatarov, B., Müller, D., Shin, D.H., Shin, S.K., Mattis, I., Seifert, P., Noh, Y.M., Kim, Y.J., Sugimoto, N., 2011. Lidar measurements of Raman scattering at ultraviolet wavelength from mineral dust over East Asia. Opt. Express 19 (2), 1569–1581. http://dx.doi.org/10.1364/OE.19.001569.

Tatarov, B., Müller, D., Tesche, M., Shin, S.-K., 2020. Lidar innovations for technologies and environmental sciences (LITES) – an remote sensing infrastructure facility: Setup and measurements examples. EPJ Web Conf. 237, 07017. http://dx.doi.org/10.1051/epjconf/202023707017.

Tatarov, B., Sugimoto, N., 2005. Estimation of quartz concentration in the tropospheric mineral aerosols using combined Raman and high-spectral-resolution lidars. Opt. Lett. 30 (24), 3407–3409. http://dx.doi.org/10.1364/OL.30.003407.

Tegen, I., Schepanski, K., 2009. The global distribution of mineral dust. IOP Conf. Ser. Earth Environ. Sci. 7, 012001. http://dx.doi.org/10.1088/1755-1307/7/1/012001.

Tesche, M., Ansmann, A., Müller, D., Althausen, D., Mattis, I., Heese, B., Freudenthaler, V., Wiegner, M., Esselborn, M., Pisani, G., Knippertz, P., 2009. Vertical profiling of Saharan dust with Raman lidars and airborne HSRL in southern Morocco during SAMUM. Tellus B: Chem. Phys. Meteorol. 61 (1), 144. http://dx.doi.org/10.1111/j.1600-0889.2008.00390.x.

Tesche, M., Tatarov, B., Noh, Y., Müller, D., 2018. Lidar sprectroscopy instrument (LISSI): An infrastructure facility for chemical aerosol profiling at the University of Hertfordshire. EPJ Web Conf. 176, 01008. http://dx.doi.org/10.1051/epjconf/201817601008.

Tirpitz, J.-L., Frieß, U., Spurr, R., Platt, U., 2022. Enhancing MAX-DOAS atmospheric state retrievals by multispectral polarimetry – studies using synthetic data. Atmospheric Meas. Tech. 15 (7), 2077–2098. http://dx.doi.org/10.5194/amt-15-2077-2022.

Weinzierl, B., Ansmann, A., Prospero, J.M., Althausen, D., Benker, N., Chouza, F., Dollner, M., Farrell, D., Fomba, W.K., Freudenthaler, V., Gasteiger, J., Groß, S., Haarig, M., Heinold, B., Kandler, K., Kristensen, T.B., Mayol-Bracero, O.L., Müller, T., Reitebuch, O., Sauer, D., Schäfler, A., Schepanski, K., Spanu, A., Tegen, I., Toledano, C., Walser, A., 2017. The Saharan aerosol long-range transport and aerosol–cloud-interaction experiment: Overview and selected highlights. Bull. Am. Meteorol. Soc. 98 (7), 1427–1451. http://dx.doi.org/10.1175/bams-d-15-00142.1.

Weitkamp, C. (Ed.), 2005. Raman lidar. In: Lidar: Range-Resolved Optical Remote Sensing of the Atmosphere. Springer New York, New York, NY, pp. 241–271. http://dx.doi.org/10.1007/0-387-25101-4_9, Chapter 9.

Wu, M., Liu, X., Yu, H., Wang, H., Shi, Y., Yang, K., Darmenov, A., Wu, C., Wang, Z., Luo, T., Feng, Y., Ke, Z., 2020. Understanding processes that control dust spatial distributions with global climate models and satellite observations. Atmospheric Chem. Phys. 20 (22), 13835–13855. http://dx.doi.org/10.5194/acp-20-13835-2020.

Yadav, A.C., Müller, D., Tatarov, B., Ghita, A., 2025. Investigation of Raman spectra of mineral dust for identifying the chemical composition of desert dust by Raman lidar. In: Scientific Research Abstracts. Vol. 15, Atmospheric Dust – Dust 2025, p. 81, Conference abstract.

Yu, H., Chin, M., Bian, H., Yuan, T., Prospero, J.M., Omar, A.H., Remer, L.A., Winker, D.M., Yang, Y., Zhang, Y., Zhang, Z., 2015. Quantification of trans-Atlantic dust transport from seven-year (2007–2013) record of CALIPSO lidar measurements. Remote Sens. Environ. 159, 232–249. http://dx.doi.org/10.1016/j.rse.2014.12.010.

Zhang, H., Wagner, F., Saathoff, H., Vogel, H., Hoshyaripour, G., Bachmann, V., Förstner, J., Leisner, T., 2022. Comparison of scanning LiDAR with other remote sensing measurements and transport model predictions for a Saharan dust case. Remote. Sens. 14 (7), 1693. http://dx.doi.org/10.3390/rs14071693.